ANALYSIS OF MEASUREMENTS
FOR SOLID STATE LASER REMOTE LIDAR SYSTEM

CONTRACT No. NAS8-38609

Delivery Order No. 77

Contract Period:
June 1, 1993 - September 31, 1994

Submitted To:

NASA/MSFC
Marshall Space Flight Center, AL 35812

Prepared By:
Farzin Amzajerdian
Center For Applied Optics
University Of Alabama In Huntsville
Huntsville, Al 35899
(205) 895-6030 ext. 452

April 7, 1995

UAH/CAO

FOREWORD

This report describes the work performed under NASA contract NAS8-38609, Delivery Order number 77, over the period of June 1, 1993 through September 31, 1994.

CONTENTS

1.0 INTRODUCTIN

The merits of using lidar systems for remote measurements of various atmospheric processes such as wind, turbulence, moisture, and aerosol concentration are widely recognized. Although the lidar technology has progressed considerably over he past two decades, significant research particularly in the area of solid state lidars remains to be conducted in order to fully exploit this technology.

The work performed by the UAH personnel under this Delivery Order concentrated on analyses of measurements required in support of solid state laser remote sensing lidar systems which are to be designed, deployed, and used to measure atmospheric processes and constituents. UAH personnel has studied and recommended to NASA/MSFC the requirements of the optical systems needed to characterize the detection devices suitable for solid state wavelengths and to evaluate various heterodyne detection schemes. The 2-micron solid state laser technology was investigated and several preliminary laser designs were developed and their performance for remote sensing of atmospheric winds and clouds from a spaceborne platform were specified. In addition to the laser source and the detector, the other critical technologies necessary for global wind measurements by a spaceborne solid state coherent lidar systems were identified to be developed and demonstrated. As part of this work, an analysis was performed to determine the atmospheric wind velocity estimation accuracy using the line-of-sight measurements of a scanning coherent lidar. Under this delivery Order, a computer database of materials related to the theory, development, testing, and operation of lidar systems was developed to serve as a source of information for lidar research and development.

2.0 CHARACTERIZATION OF DETECTORS AND HETERODYNE DETECTION TECHNIQUES

2.1 INTRODUCTIN

In support of a NASA plan for further advancing solid state laser technology for remote sensing applications, an analysis of measurements for characterization of near-infrared detection devices operating in the eye-safe wavelength region was performed and a Detector Characterization Facility (DCF) was designed to be developed at the Marshall Space Flight Center. The DCF will provide all the necessary detection parameters for design, development and calibration of coherent and incoherent solid state laser radar (lidar) systems. The coherent lidars in particular require an accurate knowledge of detector heterodyne quantum efficiency[1-3], nonlinearity properties[4-6] and voltage-current relationship[7,8] as a function of applied optical power. At present no detector manufacturer provides these quantities or adequately characterizes their detectors for heterodyne detection operation. In addition, the detector characterization facility measures the detectors DC and AC quantum efficiencies noise equivalent power and frequency response up to several GHz. The DCF will be also capable of evaluating various heterodyne detection schemes such as balanced detectors and fiber optic interferometers.

The detector characterization facility at MSFC is part of the design and development of a solid state lidar test bed. The objective of the lidar test bed and characterization facilities is to evaluate the performance of solid state lasers, detectors and other components and subsystems, both individually and in concert, operating as a coherent lidar for remote measurements of atmospheric wind and aerosol backscatter.

2.2 DETECTOR CHARACTERIZATION FACILITY

The detector characterization optical design and measurement technique are illustrated in figures 1 and 2. The measurements have been based on using two diode-pumped, single mode, continuous wave, Tm, Ho:YLF (Thulium, Holmium:YLF) lasers operating at 2 microns wavelength. Both lasers can be tuned using an intracavity etalon over a wide range of about 22 nm or 1500 GHz centered at 2060 nm. The frequency of one of the lasers can be further controlled by adjusting its resonator length using a piezoelectric (PZT) translation stage. This laser can be continuously tuned over a frequency range of about 1 GHz by applying a voltage to the PZT stage. Both lasers can produce about 100 mW of single frequency power.

Some of the detector characterization measurements require both lasers to illuminate the detector under-the-test and the rest of the measurements require the use of one of the lasers for which the output of the other lasers is blocked from entering the detector. For the measurements that require only one laser, the output of the continuously tunable laser is first measured by a precision power meter and thereafter is monitored by an InAs detector. The InAs detector has a 200 KHz bandwidth, which is more than sufficient for measuring any variation in the laser output power that may occur during the measurement procedure. The output of the InAs detector is fed into the

signal processing instrument in real time so that the measurements can be accordingly normalized. For these measurements, a short focal length lens (25 mm) is placed in front of the detector being characterized. The short focal length lens will focus the beam to a spot size considerably smaller than the detector effective area to avoid introducing any truncation error in the measurements. The detector output is then amplified by an electronic receiver to be measured and recorded by the signal processing instrument. The receiver can operate in either DC or AC-coupled mode using a manual switch and an on-line relay (figure 2). For the single laser measurements, the receiver will be operating in the DC-coupled mode.

The measurements of the detector frequency response and heterodyne quantum efficiency will require the use of both lasers. For these measurements, the outputs of the lasers are focused by two long focal length (75 cm) lenses and then combined by a beam splitter at the detector. By mixing the two laser beams, the detector generates a current that has three components. Two DC components corresponding to each beam and a AC component at the difference frequency between the two lasers. By operating the receiver in AC-coupled mode, the AC component of the detector output can be separated and amplified to be measured. By varying the frequency of the continuously tunable laser, the detector frequency response can be determined. The amplitude of the detector AC output current is directly related to the product of the DC currents due to the individual beams and the detector's heterodyne quantum efficiency. Therefore by normalizing the detector AC signal power by the amplitudes of the detector DC components, the detector heterodyne quantum efficiency can be obtained as a function of signal frequency. Since the detector frequency response is related to the bias voltage, these measurements will be repeated for different applied reverse-biased voltages.

The electronic receiver operation is critical for accurate measurements of detection parameters. The electronic receiver performs three functions: amplifying detector output current, interfacing the detector and the measurement/recording instrument, and providing bias voltage to the detector. The operation of the receiver is shown in figure 2. The receiver uses a variable voltage source for providing an adjustable bias voltage, a DC-coupled transimpedance amplifier for single laser measurements and a AC-coupled transimpedance amplifier for two lasers measurements. The transimpedance amplifiers have a moderate gain (V_{out}/I_{in}) of about 1000. In order to accurately measure the detector output current, the input impedances of both DC and AC-coupled amplifiers have been selected to be much less than the internal resistance of the InGaAs detectors that is typically of the order of 100 KΩ. This will ensure that virtually all the detector current will flow into the amplifiers. Furthermore, lower input impedance for the AC-coupled amplifier translates to wider measurement bandwidth. The AC-coupled amplifier uses a 60 Ω input impedance that will allow for frequency response measurements of up to 2 GHz. An even wider bandwidth amplifier is being considered to be designed and built in the future.

The receiver provides output ports for measuring the applied bias voltage and monitoring the current flowing through the detector. By varying the applied bias voltage and measuring the detector current, a family of V-I curves for different applied optical power can be obtained. These curves along with the detector linearity and frequency response properties are necessary for determining the detector optimum local oscillator power and bias voltage for operation in a coherent lidar system.
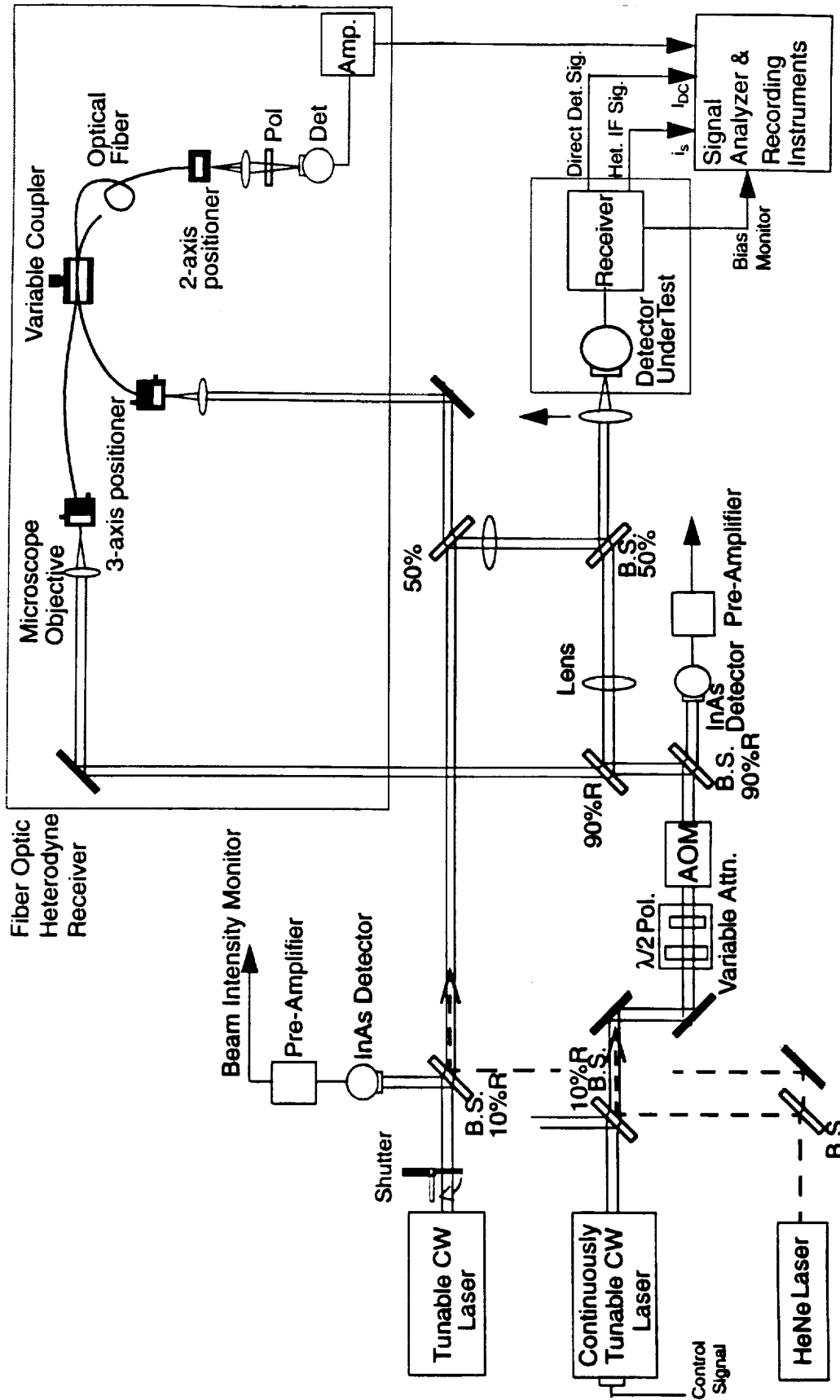
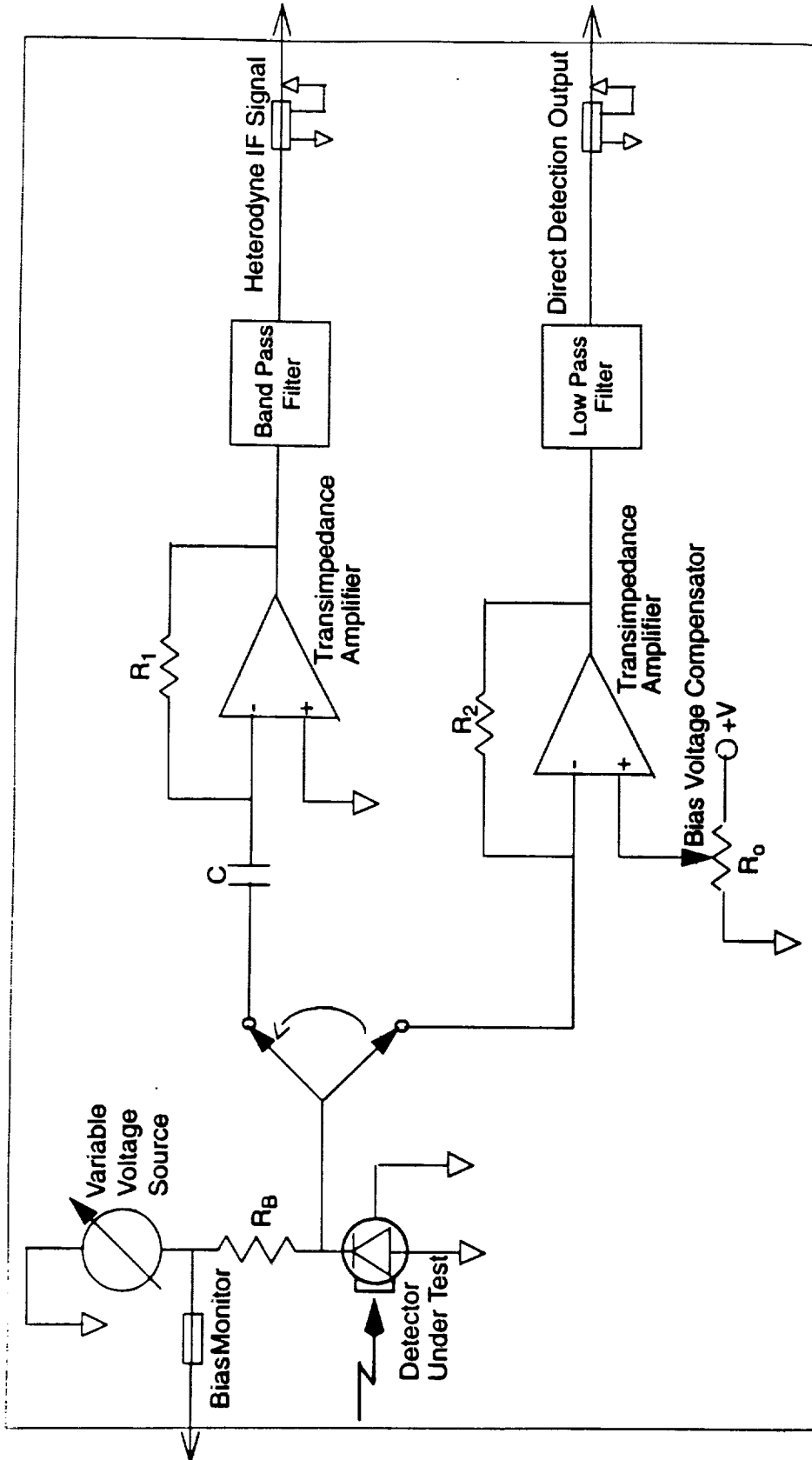Figure 1. Detector Characterization Optical System.

Figure 2. Detector Electronic Receiver

As shown in figure 1, part of each laser beam is split and directed toward a fiber optic assembly that allows the evaluation of fiber optic heterodyne receivers. The two laser beams are coupled into two optical fibers to be mixed by a variable fiber optic coupler. The output of the coupler is then directed through another optical fiber toward a detector. This fiber optic interferometer assembly is capable of characterizing the optical fiber transmission properties and the coherent mixing efficiencies of fiber optic couplers. The variable coupler used in the fiber optic interferometer assembly will also allow the optimum mixing ratio of the signal and local oscillator to be determined experimentally.

2.2.1 DIRECT DETECTION MEASUREMENTS

The detector parameters that will be measured by using a single laser beam (direct detection) are summarized in table 1. All the direct detection measurements will be performed by the continuously tunable laser without having to readjust the mirrors or beam splitters for each measurement. It is particularly undesirable to readjust the angular position of the beam splitters, since their transmission to reflection ratios have a angular dependency. The variable attenuator utilizes a combination of a half-wave plate and a polarizer to allow for controlling the laser beam power without causing the beam to deflect or translate as would be the case if neutral density filters are used. By placing or removing neutral density filters or any other form of substrates with a finite thickness during the characterization procedure, the laser beam will deviate from its original path introducing additional error in the measurements.

Table 1: Direct Detection Measurements

Parameter	Measurement
Responsivity	$\rho = \dfrac{I_d}{P_{in}}$
DC Quantum Efficiency	$\eta_{DC} = \left(\dfrac{h\nu}{e}\right)\rho$
Detector Nonlinearity	$\alpha = \dfrac{\rho P_{in} - I_d}{P_{in}^2}$
V-I Curves	$I_B = \dfrac{V_B}{R_B}$
Spectral Response	$\rho(\nu) = \dfrac{I_d(\nu)}{P_{in}(\nu)}$
Noise Equivalent Power	$NEP = P_{in}$ when $SNR = 1$

The direct detection measurements of the detectors are based on the following simple expression relating the detector output current to the applied optical power.

$$I_d = \left(\frac{e}{h\nu}\right)\eta_{DC}P_{in} \tag{1}$$

where η_{DC} is the detector DC quantum efficiency, e is electron charge, h is Planck's constant, ν is the laser frequency, P is the incident optical power and I is the detector output current. Eq. (1) can also be expressed in terms of the detector responsivity ρ

$$I_d = \rho P_{in} \tag{2}$$

Therefore by accurately measuring the laser power incident on the detector and the detector output current, the detector responsivity can be determined. Then the detector responsivity can be related to the DC quantum efficiency by

$$\eta_{DC} = \left(\frac{h\nu}{e}\right)\rho \tag{3}$$

The measurement error due to the laser beam truncation and misalignment was estimated to be less than 1% for a detector with an active area diameter of 75 μm. For most coherent lidar applications, detector sizes less than 50 μm are not practical. Therefore, the 25 mm focal length lens chosen for focusing the laser beam on the detector provides a sufficiently small spot for detector responsivity measurements. The laser beam spot size at the detector is about 40 μm in diameter.

As opposed to the direct detection lidars, for which the return signal power is usually well below the detector saturation level, the coherent lidars may require operating the detectors in their nonlinear regions because of the application of a local oscillator beam. Therefore, the knowledge of the detector nonlinearity is essential for determining the optimum local oscillator power and predicting the lidar heterodyne detection performance. The detector nonlinearity will be measured at the DCF by measuring the detector output current as a function of applied optical power. The least-squares fit of the measured data to a second degree polynomial will then provide the detector nonlinearity coefficient. A second degree polynomial, as defined below, is a reasonable model for the detector current.

$$I_d(P_{in}) = \rho P_{in} - \rho\alpha P_{in}^2 \tag{4}$$

In this expression, α is the detector nonlinearity coefficient. For low levels of optical power (Pin << 1/α), the expression above reduces to Eq. (2).

The other important quantity, that will be measured, is the detector voltage-current relationship for different optical power levels. A family of V-I curves will be generated for each detector under consideration for use in coherent lidar systems. this will be performed by measuring the current flowing through the detector as a function of applied voltage across the detector for different applied optical power levels. The V-I curves are necessary for specifying the detector optimum bias voltage as well as the optimum local oscillator power.

The DCF measurements of the detector spectral response will be limited to the tuning range of the laser (22 nm), which is much narrower than the typical spectral response of semiconductor detectors. The spectral response of semiconductor detectors are typically several hundreds of nanometers and very much constant over tens of nanometers. The primary spectral region of interest for the solid state coherent lidars is from 2020 nm to 2090 nm. For other applications that full spectral response measurements are required, a blackbody source of radiation, as described later in this section, will be utilized. Blackbodies inherently generate infrared radiation over a very wide spectral range of several micrometers.

In the optical system of figure 1, the Acousto-Optic Modulator (AOM) is used as an intensity modulator for noise equivalent power measurement. The AOM is driven by a fixed RF frequency signal modulated by an adjustable amplitude and frequency signal. The AOM in turn modulates the laser beam intensity eliminating the need for using a mechanical chopper which can degrade the measurement accuracy. The chopper transmission function is highly variant depending on the position of the beam on the chopper wheel and its rotation frequency. Therefore, using a mechanical chopper would require frequent calibration that are tedious to perform and can affect the measurements repeatability.

2.2.2 HETERODYNE DETECTION MEASUREMENTS

For the heterodyne detection measurements, the short focal length lens immediately in front of the detector is removed from the optical path. First, the detector DC currents due to each beam are measured individually. At this stage, the receiver is set to operate in the DC-coupled mode. Then, the receiver is switched to the AC-coupled mode and both beams are allowed to illuminate the detector. The two laser beams are combined by a 50% beamsplitter and directed toward the detector. The detector in turn generated a signal with a frequency equal to the frequency difference between the two beams. The amplitude of this signal is directly related to the product of the DC currents due to the individual beams and the detector's heterodyne quantum efficiency.

Initially, the frequencies of the lasers are adjusted to within tens of MHz of each other using the wavelength control etalons. The measurements are then performed by varying the frequency of the continuously tunable laser and recording the receiver output voltage that is directly proportional to the magnitude of the heterodyne signal. The coarse laser frequency adjustment is performed by the intracavity etalon and the fine adjustment by the cavity length control PZT.

The heterodyne detection measurements can be best described by the heterodyne detection equation below that relates the detector output current (i_h) to the laser beams powers, P_1 and P_2, incident on the detector.

$$i_h(f) = 2\left(\frac{e}{h\nu}\right)\eta_{AC}(f) F_0^{1/2} \sqrt{P_1 P_2}\cos(\omega_1 - \omega_2) \tag{5}$$

Where ω_1 and ω_2 are the corresponding laser frequencies, η_{AC} is the detector AC quantum efficiency at frequency $f = 2\pi(\omega_1 - \omega_2)$, and F_0 is the signal power reduction factor that accounts for

the loss of signal power due to imperfect wavefronts matching and optical misalignment. Taking the mean-square of the heterodyne current, we obtain the heterodyne signal power.

$$\overline{i_h^2(f)} = 2\left(\frac{e}{h\nu}\right)^2 \eta_{AC}^2(f)\, F_0 P_1 P_2 \tag{6}$$

Normalizing Eq. (6) by the individual DC currents due to P1 and P2 given by Eq. (1), we can write

$$\frac{\overline{i_h^2(f)}}{I_{DC1}I_{DC2}} = \frac{2\eta_{AC}^2(f)}{\eta_{DC}^2} F_0 \tag{7}$$

The AC heterodyne quantum efficiency is then equal to

$$\eta_{AC}(f) = \left(\frac{\overline{i_h^2(f)}}{2I_{DC1}I_{DC2}}(\eta_{DC}^2/F_0)\right)^{1/2} \tag{8}$$

where the signal reduction factor F_0 can be set equal to 1 for the DCF optical system (figure 1). As explained later in this section, any reduction in the heterodyne signal power due to the optical misalignment and beams wavefronts mismatch will be negligible and F_0 will be essentially unity for the DCF heterodyne detection measurements. Therefore by quantifying the detector DC quantum efficiency as described earlier and measuring the heterodyne signal power and the direct detection DC currents due to the individual beams, the AC quantum efficiency of the detector can be obtained. The heterodyne signal power and the DC currents are related to the receiver output voltages as:

$$i_h^2 = \frac{\overline{V_{out}^2}}{g_{AC}^2(f)}$$

$$I_{DC} = \frac{V_{out}}{g_{DC}}$$

where g_{AC} and g_{DC} are the receiver AC and DC gains.

For an ideal shot noise-limited coherent lidar, the signal to noise ratio (SNR) is equal to

$$\frac{S}{N} = \frac{\eta_{AC}^2 \eta_H P_s}{\eta_{DC} h\nu B_{IF}} \tag{9}$$

where η_H is the heterodyne mixing efficiency and P_s is return signal power. The coherent lidar SNR is often written as

$$\frac{S}{N} = \frac{\eta_{HQE}\eta_H P_s}{h\nu B_{IF}} \tag{10}$$

where the quantity η_{HQE}, referred to as the "detector heterodyne quantum efficiency", is equal to

$$\eta_{HQE} = \frac{\eta_{AC}^2}{\eta_{DC}} \tag{11}$$

In Eq. (10), η_H is a system parameter that quantifies the lidar optical heterodyne efficiency while η_{HQE} is a detector parameter that quantifies the efficiency of the detector in generating an AC electrical current at the difference frequency between the local oscillator and signal beams frequencies. Substituting Eq. (8) in Eq. (11), the detector heterodyne quantum efficiency can be written in terms of the measured detector output currents.

$$\eta_{HQE}(f) = \frac{\overline{i_h^2(f)}}{2I_{DC1}I_{DC2}}(\eta_{DC}/F_0) \tag{12}$$

The other parameter that will be obtained using heterodyne detection measurements is the detector frequency response as a function of applied bias voltage. The detector frequency can be defined as

$$H(f, V_B) = \frac{\eta_{AC}(f, V_B)}{\eta_{DC}} \tag{13}$$

where V_B is the applied bias voltage across the detector. Using Eq. (8), the detector frequency response can be written as

$$H(f, V_B) = \left(\frac{\overline{i_h^2(f, V_B)}}{2F_0 I_{DC1}I_{DC2}}\right)^{1/2} \tag{14}$$

As mentioned earlier, the signal power reduction factor F_0 accounts for any reduction in the detector signal power due to the laser beams misalignment and displacement of reflective and focusing optics. However, the DCF optical system has been designed such that the measurement will not be sensitive to the optical alignment and F_0 can be set equal to unity in the expressions above. The DCF optical design has been based on the results of an analysis that was performed to formulate the signal reduction factor.

By using the Huygens-Fresnel principle and performing some tedious mathematical manipulations, a general formulation for the signal power reduction factor F_0 for two guassian laser beams was derived that can be expressed in the following form

$$F_0 = \frac{\alpha^4/\alpha_1^2\alpha_2^2 + 2(\alpha/\beta_0)^2 + (\alpha/\beta_0)^4}{(1 + (\alpha/\beta_0)^2)^2} EXP\left[-\frac{(\alpha^4/4)(k^2 S^2 + k^2 a_f^2 - 2k^2 \vec{a}_f \cdot \vec{S} - 16a_n^2)}{(1 + (\alpha/\beta_0)^2)}\right]$$

(15)

where

$$\alpha^2 = \frac{2\alpha_1^2\alpha_2^2}{\alpha_1^2 + \alpha_2^2}$$

$$\vec{a}_f = \frac{\vec{a}_1}{R_1} - \frac{\vec{a}_2}{R_2}$$

$$2\vec{a}_n = \frac{\vec{a}_1}{\alpha_1^2} - \frac{\vec{a}_2}{\alpha_2^2}$$

$$\vec{S} = \vec{S}_1 - \vec{S}_2$$

k is the wavenumber of the laser beams, β_0 is the detector active area radius, α_1 and α_2 are the beams radii at the detector plane, R_1 and R_2 are the beams radius of curvatures, vectors a_1 and a_2 specify the transverse positions of the beams in the plane of the detector, and vectors S1 and S2 are the beams pointing vectors specifying their propagation directions.
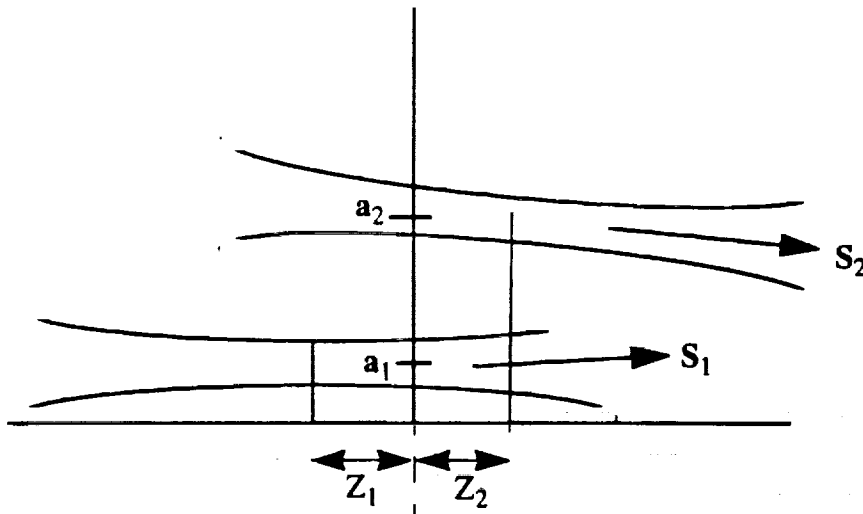

Figure 3. The beam waist location of each beam with respect to the detector.

As shown in figure 3, the locations of the beams focal points along the optical axis are specified by Z_1 and Z_2. By taking advantage of the fact that the laser beams can be easily focused on the detector to within the Rayliegh range (Z_1 and $Z_2 < Z_R$), Eq. (15) can be reduced to

$$F_0 = EXP\left[-\frac{k^2\alpha_0^2 S^2/4 + a^2/\alpha_0^2 + \frac{4}{k^2\alpha_0^6}(W\vec{a} + Z\vec{q})^2 - 2/\alpha_0^2(W\vec{a}\cdot\vec{S} + Z\vec{q}\cdot\vec{S})}{(1 + (\alpha/\beta_0)^2)}\right] \qquad (16)$$

where

$$\vec{a} = \vec{a}_1 - \vec{a}_2 \qquad\qquad Z = Z_1 - Z_2$$

$$\vec{q} = \frac{\vec{a}_1 + \vec{a}_2}{2} \qquad\qquad W = \frac{Z_1 + Z_2}{2}$$

For the DCF, two relatively long focal length (75 cm) lenses have been selected to focus the laser beams on the detector. The long focal length lenses ensure that the spot size of each beam is considerably larger than the detector area. The diameter of each laser beam at the detector plane is about 1mm while the detectors active area diameters are usually of the order of 0.1 mm. The combination of larger spot sizes and more uniform wavefronts along the propagation path, allow for a relaxed beam position and pointing alignment tolerances and a high mixing efficiency. Figure 4 illustrates the dependence of the Signal Power Reduction Factor on the beams spot sizes at the detector plane. Figure 5 shows the measurements insensitivity to defocusing of the beams. The results of figures 4 and 5 have been obtained by evaluating Eq. (16) using realistic system parameters.
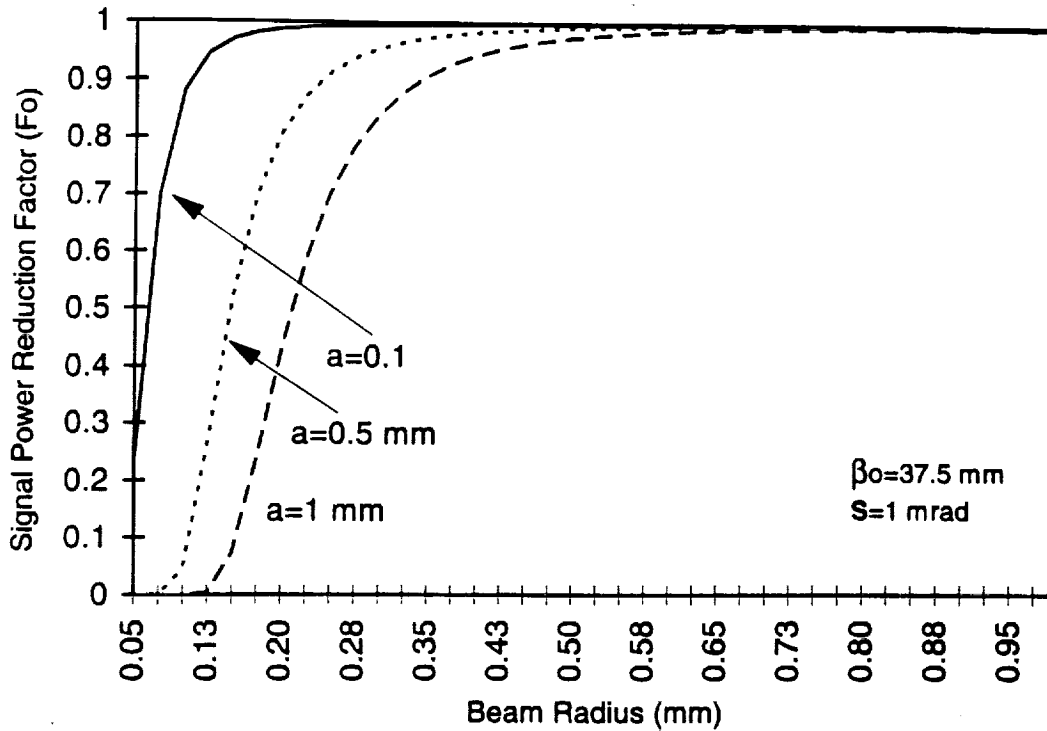
Figure 4. Signal Reduction Factor as a function of beam radius at the detector.
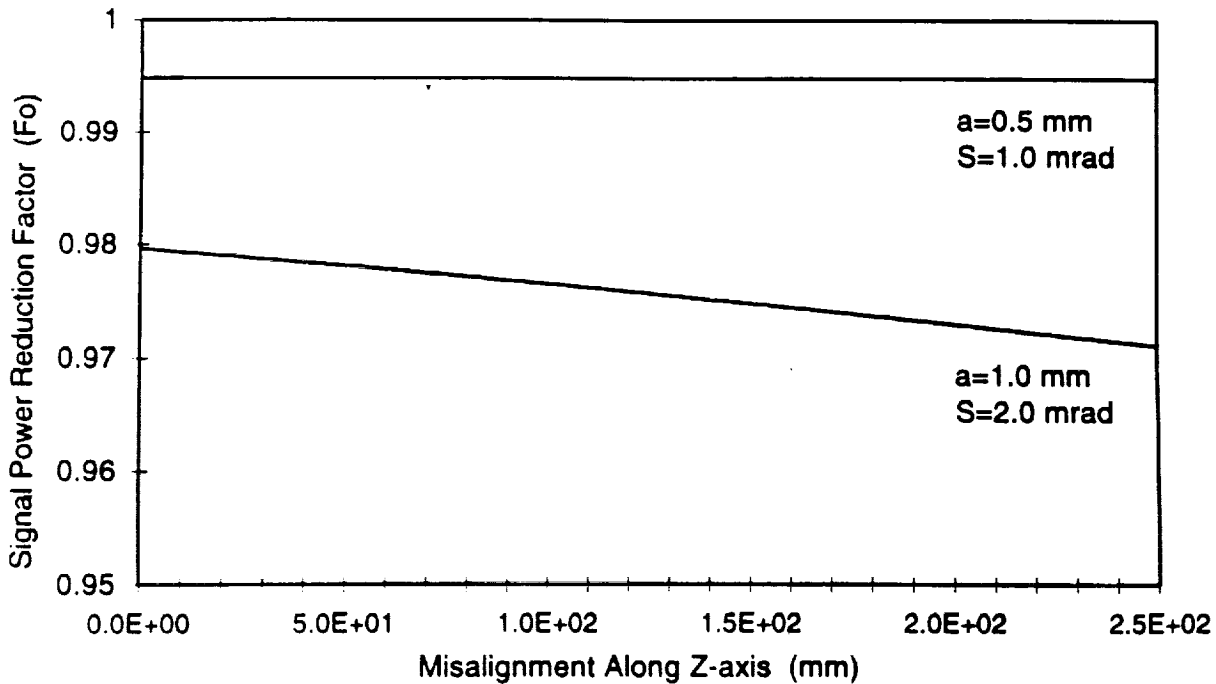

Figure 5. Effect of defocusing/longitudinal beam misalignment on the DCF heterodyne detection measurements, for a beam waist radius of $\alpha_0=0.656$ mm and detector active area radius of $\beta_0=37.5$ μm.

As can be seen from figure 5, the heterodyne measurements are very much insensitive to longitudinal beam position misalignment or defocusing of the beams. Therefore the last two terms in the exponent of Eq. (16), which account for the defocusing error, can be ignored for the DCF measurements. Then by using the fact that $\alpha^2_0 >> \beta^2_0$, Eq. (16) will be greatly simplified as following.

$$F_0 = EXP\left(-\frac{k^2\beta_0^2 s^2}{4} - \frac{a^2\beta_0^2}{\alpha_0^4}\right) \qquad (17)$$

Eq. (17) has been shown in figures 6 and 7 for α_0=0.656 mm and β_0=37.5 μm. As can be seen from figure 6, the measurements are also fairly tolerable toward beam pointing errors and transverse deblackbodypositioning of the beams on the detector. Figure 7 indicates that the error due the optical misalignment and imperfect wavefront matching will be about 2% for a position misalignment tolerance of +/-1 mm and an angular tolerance of +/-2 mrad. It should be noted that these misalignment tolerances can be achieved by using a HeNe laser and the conventional alignment techniques.
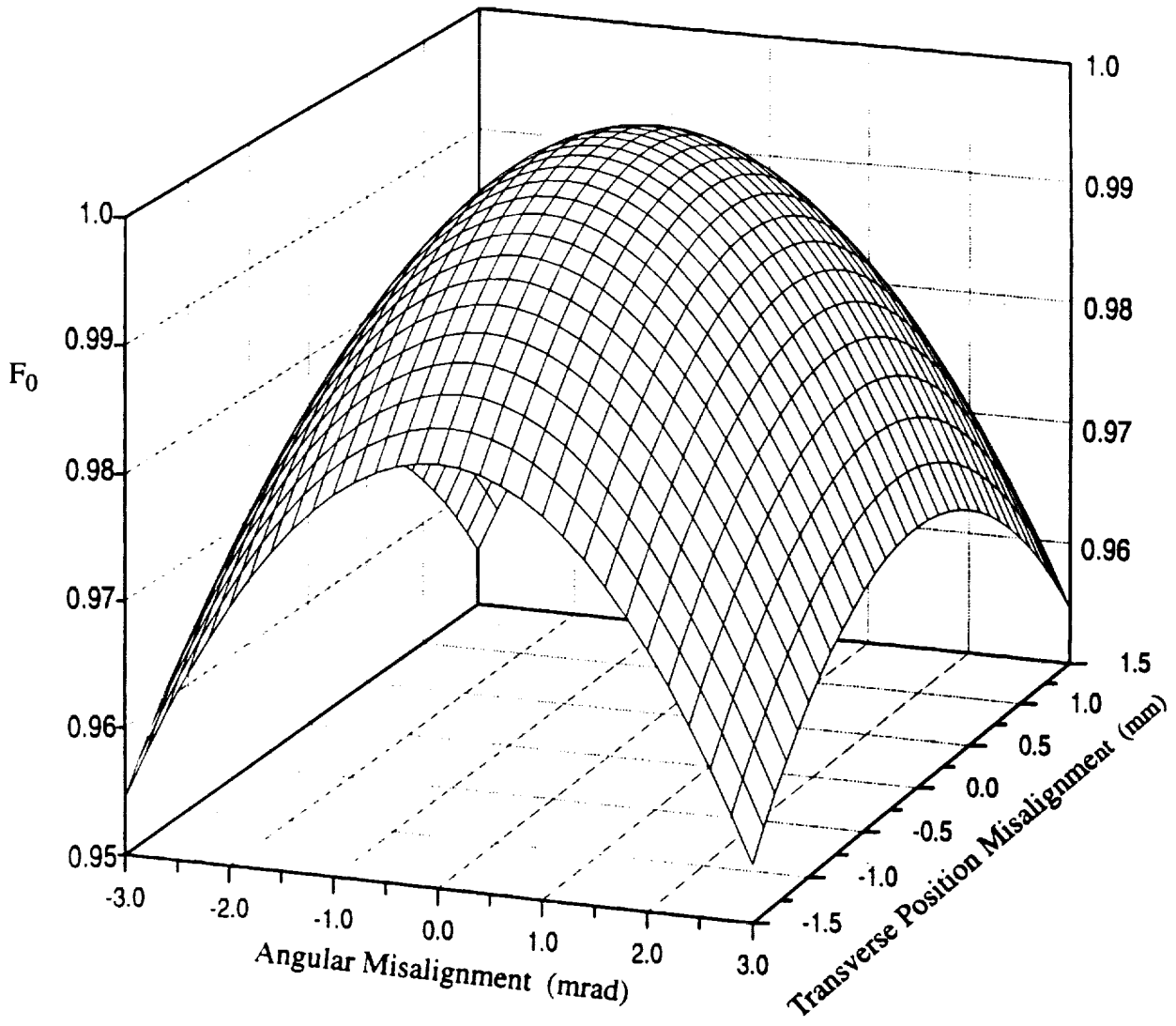
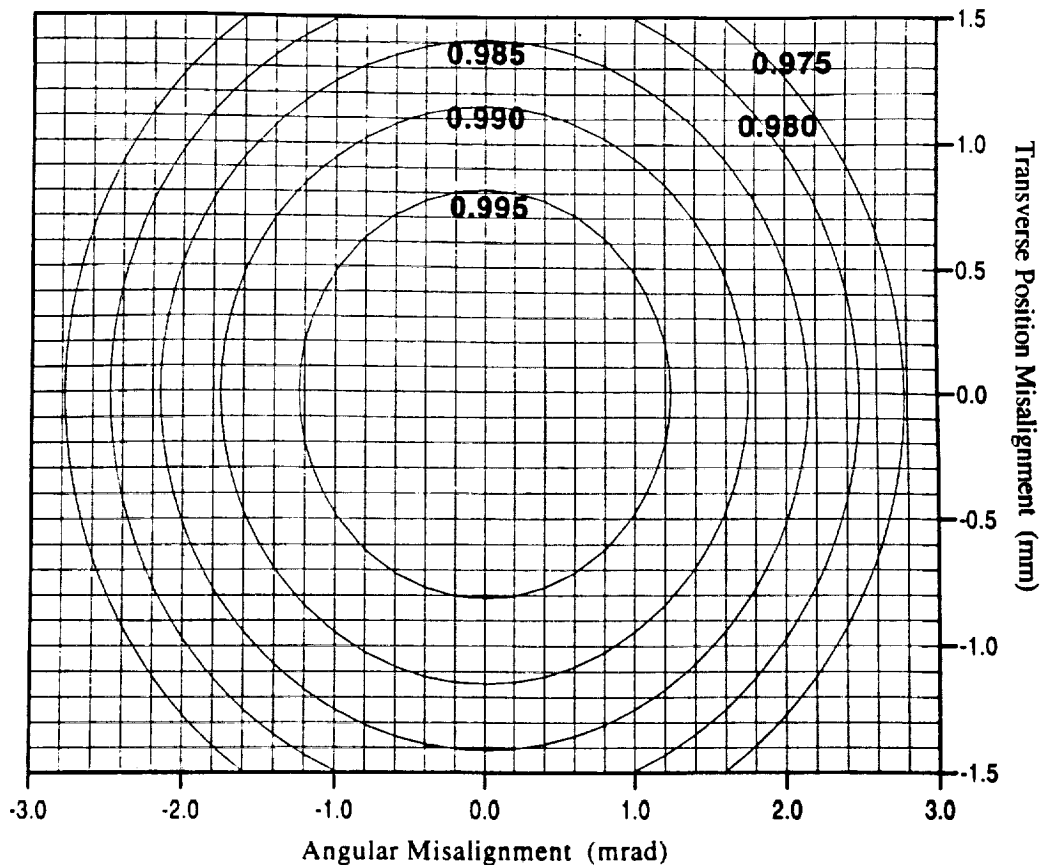Figure 6. Signal Reduction Factor as a function of beams transverse depositioning and pointing errors.

Figure 7. Contours of Signal Reduction Factors.

2.2.3 FIBER OPTIC HETERODYNE RECEIVER

In view of increasing interest in utilizing the fiber optic technology in coherent lidar systems for coherent mixing of the signal and local oscillator beams, an analysis of measurements for characterization of optical fibers and couplers was performed. Compared with more conventional technique of mixing signal and local oscillator beams using dichroic optical elements, fiber optic technology allows for a less alignment sensitive design. The other advantage of the "fiber optic heterodyne receivers" is their modular design that can provide considerable flexibility in positioning the lidar receiver assembly independently from of the rest of the lidar system (see figure 8). The trade-offs are attenuation in the optical fiber, coupler insertion loss and the signal beam to fiber coupling loss. Maintaining the signal and local oscillator polarizations through the fiber and matching them with each other at the coupler are the main challenges in deigning fiber optic heterodyne receivers.
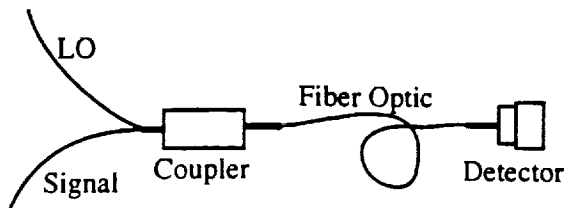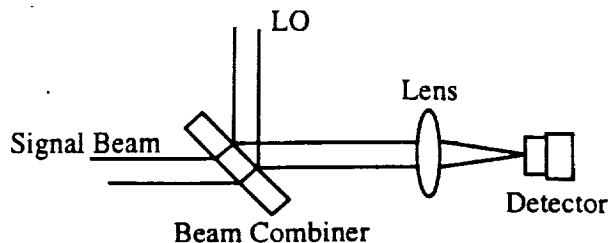
Figure 8. Fiber optic and conventional heterodyne receivers.

As shown in figure 1, the fiber optic receiver measurement system has been designed such that it can directly be incorporated into the detector characterization facility. This measurement system is capable of characterizing the optical fiber transmission properties and the heterodyne mixing efficiencies of fiber optic couplers. A variable coupler has been used to allow the optimum mixing ratio of the signal and local oscillator to be determined experimentally for different detection parameters.

In the measurement system of figure 1, part of each laser beam has been split and directed toward the ends of the two optical fibers. The fibers are single mode and polarization maintaining with a core diameter of about 10 μm. The optical fibers direct the beams to a coupler where they are coherently mixed. The output of the coupler is transmitted through another fiber to a InGaAs detector. The detector output is then amplified by a wide bandwidth (1 GHz), DC-coupled amplifier to be measured and recorded by a fast digital oscilloscope.

To characterize the fiber optic receivers, first the detector output due to each beam is measured individually. Then the amplitude of the heterodyne signal resulting from mixing of both beams is measured. The measured detector DC signals due to the individual beams are used to specify the optical fibers transmission, the coupler insertion losses and the losses associated with the coupling of the laser beams into the fibers. The measured heterodyne signal then allows to quantify the heterodyne mixing efficiency η_{Hf} of the fiber optic receiver. The receiver heterodyne mixing efficiency is related to the measured detector output currents by

$$\eta_{Hf} = \frac{\overline{i_h^2}}{2I_{DC1}I_{DC2}}(\eta_{DC}/\eta_{AC})^2 \qquad (18)$$

As can be seen from Eq. (18), these fiber optic receiver measurements require prior knowledge of the detector AC and DC quantum efficiencies and the amplifier gain. In addition to characterization of fiber optic receivers, this setup allows the optimum mixing ratio of signal and local oscillator beams to be determined experimentally. This is achieved by changing the mixing ratio, by the variable coupler used in this setup, and measuring the corresponding heterodyne signal.

2.3 BLACkBODY DETECTOR MEASUREMENTS

Blackbodies are commonly used for characterization and calibration of infrared sensors and detectors as a cost effective means of generating infrared radiation over a wide spectral range. Earlier work on the characterization of detectors for optical heterodyne detection operation at 10 microns wavelength have also used blackbodies as the source of radiation[9-11]. However, the accuracy of the blackbody measurements of detection devices are limited because of very low amount of radiation that effectively illuminate the detector. An analysis was performed to evaluate the use of a blackbody as the source of radiation for characterizing the 2-micron detectors. It was concluded that the accuracy of the direct detection measurements of 2-micron detectors using blackbody sources will be compatible with that of longer wavelength infrared detectors, while the heterodyne detection measurements will be substantially less accurate. As compared with the two lasers technique described in previous section, the blackbody measurements have several disadvantages. Of course, the low signal-to-noise ratio associated with the blackbody measurements is one of the major disadvantages. Another disadvantage of blackbody measurements is the need for a tedious calibration procedure before each measurement that results in inconsistent and unreliable data. The other disadvantage is the inability to provide the detector heterodyne quantum efficiency at discrete frequencies. Finally, a blackbody measurement system is not as flexible of the two lasers system for evaluating different heterodyne detection techniques such as fiber optic interferometry, balanced detectors, and detector arrays. The major advantage of the blackbody measurements is the ability to provide the detector responsivity over very wide spectral range. The spectral range measurement by the two laser technique is limited to about 20 nm, while black bodies radiates over several micrometers.

Since a well calibrated blackbody source and all the necessary equipment for the blackbody measurements are presently available at MFSC, it has been recommended that a blackbody measurement system to be developed as a companion to the two lasers system described in the earlier sections. Such a back body measurement system can be used for measuring the full spectral range of detectors, when it is required. In addition the blackbody measurements can be used for independently verifying the two lasers measurements.

2.3.1 MEASUREMENT SYSTEM

Figures 9 illustrates the design of the blackbody measurement system. Similar to the two laser system, the blackbody system can operate in both direct and heterodyne detection modes. The thermal radiation from the blackbody source is first pass through a bandpass optical filter and then intensity modulated by a chopper before being focused on the detector by a 75 mm focal length lens. For the heterodyne detection measurement, part of the continuously tunable laser output is allowed to mixed with the blackbody radiation by the detector. A 10% beamsplitter that is placed in front of the laser (see figure 1) directs sufficient local oscillator power for this measurement. The laser beam and the blackbody radiation are combined and directed toward the detector by another 10% beamsplitter (see figure 9). For this measurement, a low-noise, wideband (~2 GHz) amplifier is used to amplify the detector output. The output of the amplifier is rectified and

filtered by a square-law detector and fed into a lock-in amplifier. The lock-in amplifier, operating at a relatively long time constant of the order of 10 msec, is synchronized with the chopper. The output of the lock-in amplifier is then measured and recorded by a digital oscilloscope. The optical filter placed has been placed along the field of view of the detector to limit the total blackbody radiation focused onto the detector. The filter has a bandwidth of about 80 nm centered at 2070 nm.
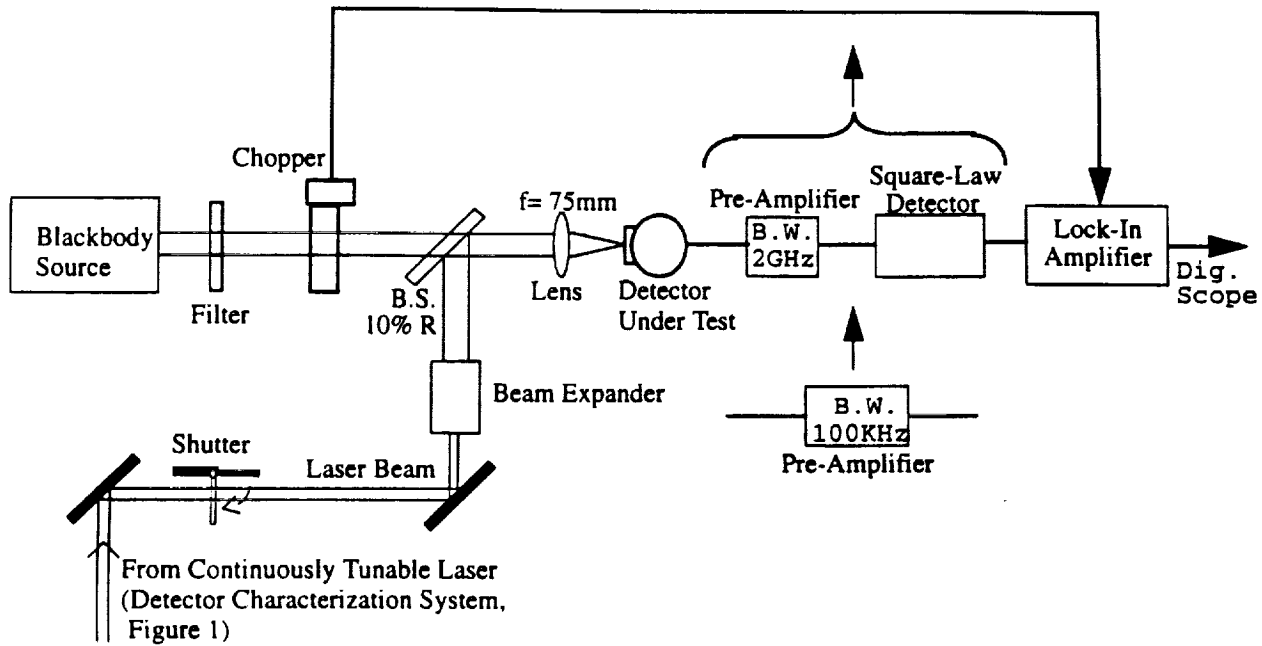

Figure 9. Blackbody detector measurement system design.

For spectral response measurement, the laser beam path to the detector is blocked and the beamsplitter is removed from the field of view of the detector, and the wideband pre-amplifier and the square-law detector are replaced by a 100 KHz pre-amplifier. The blackbody radiation still passes through the chopper and is focused on the detector by the 75 mm focal length lens. For this measurement, the output of the lock-in amplifier is measured as the different optical filters with different center wavelengths are placed along the detector field of view. Each filter has a bandwidth of about 80 nm with center wavelengths ranging from 1700 nm to 2200 nm.

2.3.2 PERFORMANCE OF BLACKBODY MEASUREMENTS

The blackbody irradiance is given by[12]

$$I_B(v) = \frac{2\pi h v^3}{c^2 (e^{hv/KT_B} - 1)} \tag{19}$$

where h is Plank's constant, v is the radiation frequency, c is speed of light, K is Boltzmann's constant, and T_B the blackbody temperature. The total power collected by the detector is then equal to

$$P_s = A\Omega \frac{2hv_0^3\Delta v}{c^2(e^{hv_0/KT_B} - 1)}$$ (20)

where A the area of the collecting aperture, Ω is the detector field of view, v_0 is the radiation center frequency received by the detector, and Δv is the bandwidth of the optical filter. For the system of figure 9, the signal power is about 2×10^{-7} W for a blackbody temperature of 1100°K. Figure 10 shows the direct detection signal power received from a 1100°K blackbody source as a function of wavelength. The signal power is normalized by the detector field of view, area and spectral bandwidth so that the blackbody measurements at 2 microns wavelength can be directly compared with operation at other infrared wavelengths. The major sources of noise for direct detection are the detector dark current noise, detector load Johnson noise and the amplifier noise. The signal-to-noise ratio seen by the pre-amplifier is therefore equal to

$$\frac{S}{N} = \left(\frac{e\eta_{DC}}{hv_0}\right)^2 \frac{A_f^2 P_s^2}{2eI_DB + 4KTB/R_L}$$ (21)

where A_f is the filter transmission factor. For for a typical 0.1 mm, InGaAs detector, the dark current I_D is about 100 nA, and the detector load resistance is 1 kΩ. Using these values in Eq. (21), the signal-to-noise ratio for the direct detection measurement is expected to be about 25 db, which is sufficient for measuring the detector spectral response. Therefore, the dominating source of error for direct detection blackbody measurement will be the system calibration error.

For the heterodyne detection, the signal power at the output of the detector can be written as

$$\bar{i_h^2} = \left(\frac{2e\eta_{AC}}{hv_0}\right)^2 \langle\left|\int d^2\vec{\rho}\, U_s(\vec{\rho})\, U^*_{LO}(\vec{\rho})\right|^2\rangle$$

$$= \left(\frac{2e\eta_{AC}}{hv_0}\right)^2 \frac{1}{\tau} \int_{t_0-\tau/2}^{t_0+\tau/2} dt \iint d^2\vec{\rho_1}d^2\vec{\rho_1}U^*_{LO}(\vec{\rho_1})\, U_{LO}(\vec{\rho_2})\, \langle U_s(\vec{\rho_1}, t)\, U^*_s(\vec{\rho_2}, t)\rangle$$ (22)

where the product of the signal and local oscillator fields has been integrated over the receiving aperture. The signal field can be expressed in terms of the field at the blackbody by using the Huygens-Fresnel principle.

$$U_s(\vec{\rho}, t) = \int dv H(v) \frac{v}{Lc} \int d^2\vec{r} U_B(v) e^{i\frac{\pi v}{Lc}(\vec{r}-\vec{\rho})^2} e^{i2\pi v(t-L/c)}$$ (23)

Where $H(v)$ is the product of the detector and the preamplifier frequency response functions.

Substituting Eqs. (19) and (23) in Eq. (22) and using the inequalities $B_{IF} << \nu_0$ and $hB_{IF} << KT$, which basically apply to all passive infrared heterodyne detection systems, the integration can be performed in closed form, giving

$$i_h^2 = \left(\frac{e\eta_{AC}}{h\nu_0}\right)^2 4h\nu_0 P_{LO} B \sum_{n=1}^{\infty} e^{-nh\nu_0/KT_B}$$

$$= \left(\frac{e\eta_{AC}}{h\nu_0}\right)^2 \frac{4h\nu_0 P_{LO} B}{(e^{h\nu_0/KT_B} - 1)} \tag{24}$$

Using eq. (24), the signal-to-noise ratio of the measurement system can be written as

$$\frac{S}{N} = \eta_{HQE} \frac{2A_t A_c}{(e^{h\nu_0/KT_B} - 1)} \left(\frac{1}{1 + 2(h\nu_0/e^2\eta_{DC}P_{LO})(KT/R_L)}\right) \tag{25}$$

Where A_t is the optical transmission of the system including the optical filter and A_c is the chopper transmission factor described later in this section. The last quantity in Eq. (25) accounts for the detector load Johnson noise, which approaches unity for smaller bandwidths. As IF signal bandwidth decreases, the detector load resistance can be increased in order to reduce the Johnson noise. For typical InGaAs detector parameters, the Johnson noise for IF bandwidths less than about 200 MHz can be ignored. It should be noted that the amplifier noise and the temperature fluctuations of the blackbody have been ignored in the expression above. For InGaAs detectors operating in 2-micron region, the signal-to-noise ratio will be less than -30 db.

The signal-to-noise ratio measured at the output of the lock-in amplifier (figure 9) is related to Eq. (25) by

$$\left(\frac{S}{N}\right)_v = g\sqrt{\frac{B}{2B_0}}\frac{S}{N} \tag{26}$$

where g and B_0 are the lock-in amplifier gain and bandwidth. Assuming S/N=-30 db, g=0.1, B=2 GHz, and B_0=10 Hz, the measured signal-to-noise ratio will be 0 db,i.e., $(S/N)_v$=1. Of course a unity signal-to-noise ratio is still insufficient for the detector heterodyne quantum efficiency measurements. To improve the measurement performance, the lock-in amplifier bandwidth need to be lowered to about 1 Hz.

Figure 10 illustrates the shot noise-limited heterodyne detection performance as function of operating wavelength. Despite low signal-to-noise ration, the blackbody heterodyne detection technique has been used in the past for measuring the averaged heterodyne quantum efficiency of 10-micron detectors. Operating at 2 microns, the blackbody measurement of the detector heterodyne quantum efficiency is even less accurate. As can be seen from figure 10, the signal-to-noise ratio at 2 micron is about 25 dB lower than 10 micron signal-to-noise ratio. As

mentioned earlier, another disadvantage of using blackbody technique is that it does not provide the detector heterodyne quantum efficiency at discrete frequencies over the IF signal bandwidth. The averaged heterodyne quantum efficiency provided by blackbody measurement is of limited use for design and analyses of solid state coherent lidars.
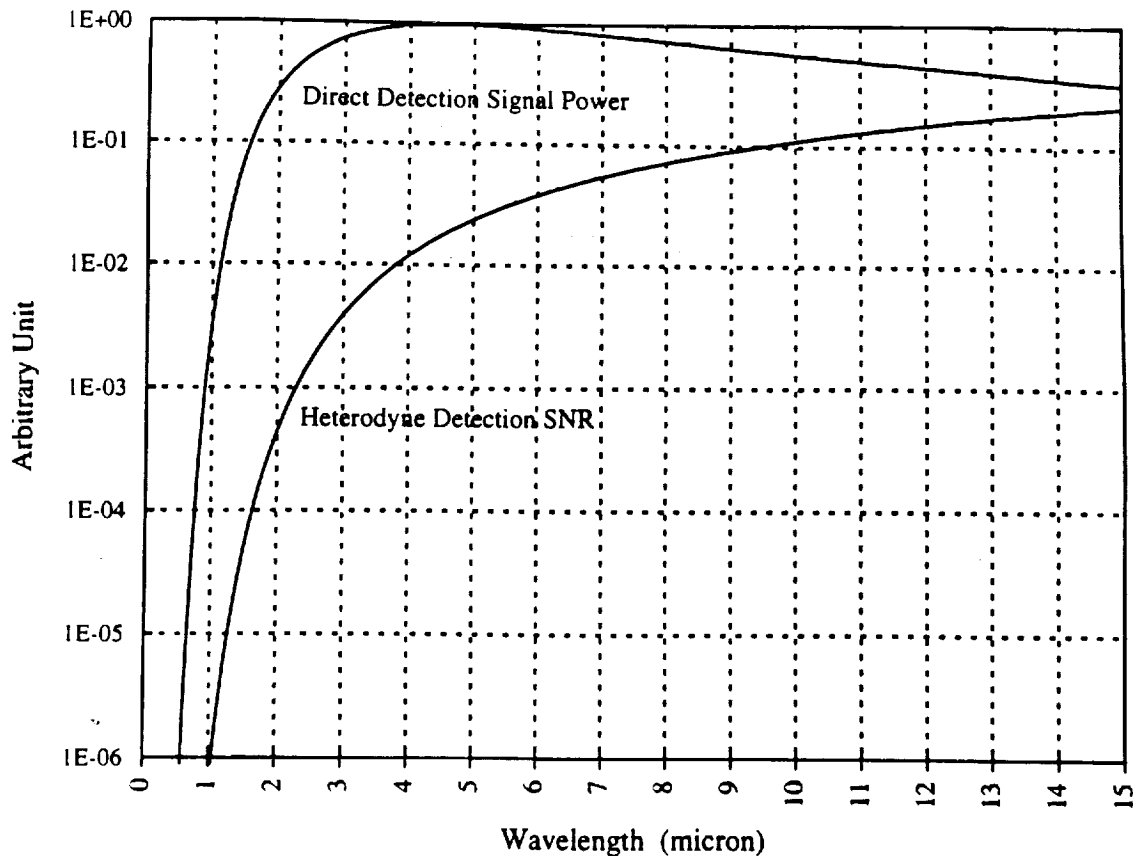

Figure 10. Performance of Blackbody Measurements

The chopper transmission factor A_c, included in Eq. (25), accounts for the fraction of the blackbody radiation that passes through the chopper and effectively mixes with the back-propagated local oscillator. Therefore, the effective aperture at the chopper is the back-propagated (BP) local oscillator pattern superimposed on the effective blackbody radiation that falls within the detector field of view (FOV). As the chopper blades pass over the superimposed BP local oscillator and blackbody aperture subtended within the detector FOV, it creates a time varying transmission function. As can be seen from figure 11, the chopper transmission function is a strong function of the relative positions of the BP local oscillator beam and the effective blackbody aperture seen by the detector with respect to each other and the center of the chopper. The chopper transmission function is also a function of the BP local oscillator beam size and the effective blackbody aperture size at the chopper plane. Therefore, it is necessary to calibrate the measurement system and measure the chopper transmission factor each time a detector is to be characterized. Obviously, the need to calibrate the chopper transmission for each detector is

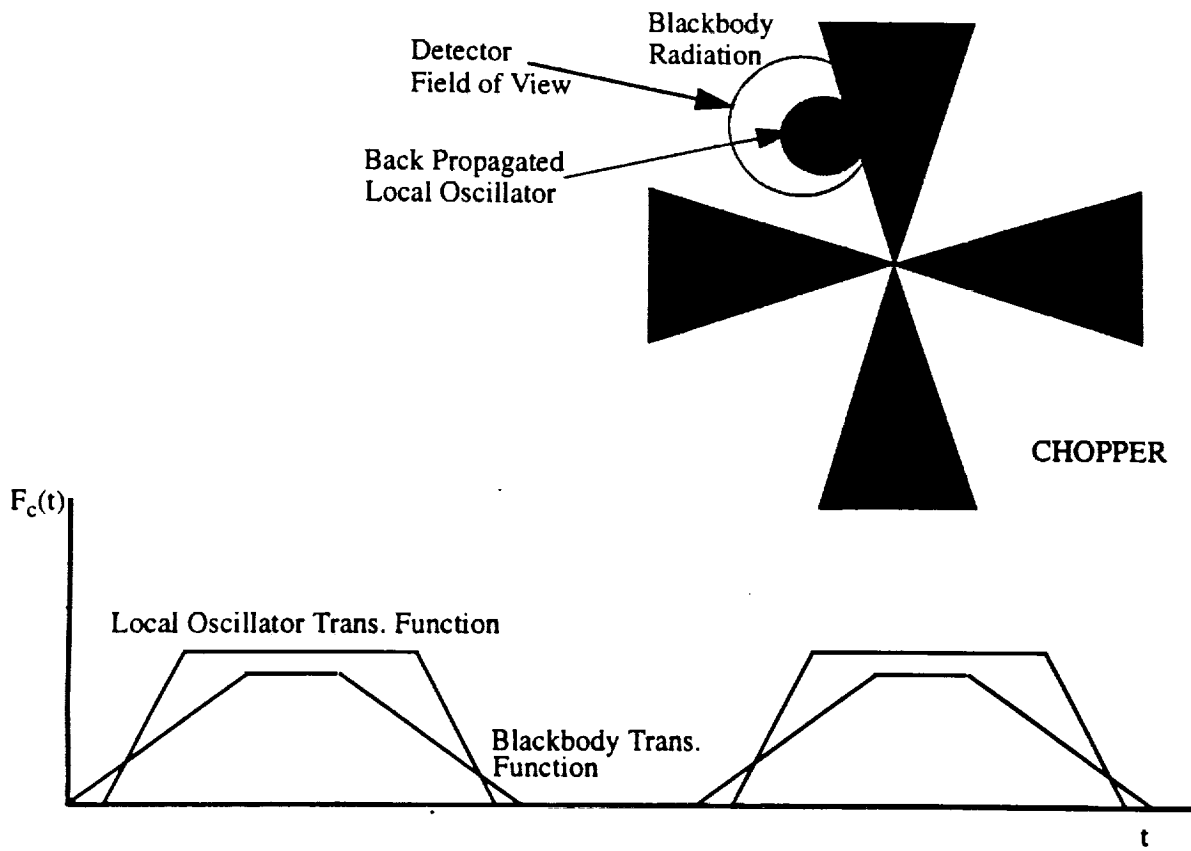undesirable since it can introduce inconsistency in the measurements.

Figure 11. Chopper Transmission Function.

3.0 SOLID STATE LASER DESIGNS FOR COHERENT LIDARS OPERATING FROM A SMALL SATELLITE

3.1 INTRODUCTIN

A number of solid state laser design concepts were developed and specified to be used as the basis for performing design trade-off analyses and establishing a series of point designs for a low cost and low risk space-based coherent Doppler lidar instrument capable of demonstrating the technology readiness for full-scale global wind measurement missions. This instrument, code-named AEOLUS (Autonomous Earth Orbiting Lidar Utility Sensor), has been proposed as the first mission for measuring atmospheric winds from space by a lidar system[13]. AEOLUS design points have been driven by the present laser and detector technologies and the constraints of small satellites. AELOUS has been designed to be self-contained and modular so that it can be accommodated by various space platforms such as the space shuttle, space station, and the small satellites that can be launched by Pegasus and Taurus class vehicles. In addition to measuring the wind fields in the high backscatter regions of the atmosphere and the cloud tops that has valuable scientific information, AELOUS will demonstrate the space operation of the key coherent lidar technologies for future full-scale missions. These key technologies include:

- Stable 2-micron, Diode-pumped, Pulsed, Solid State Laser Operation In Space
- Autonomous Laser Single Frequency Operation
- Platform Induced Doppler Frequency Shift Compensation
- Relative Alignment of Back-Propagated Local Oscillator and Return Signal Beams
  - Return Signal Lag Angle Compensation
  - Return Signal Beam De-Rotation
- Accurate Telescope Scanning and Pointing
- Lidar Calibration In Space And Active Alignment Control
- Heat Management And Temperature Control

As part of this effort, the present state of the 2-micron, solid state laser technology was investigated and the designs of the existing commercial and laboratory type lasers were evaluated. Based on this study, a number of laser system design concepts suitable for AEOLUS project were developed. These laser designs, that use commercial off-the-shelf components, can be implemented and tested for space operation in less than 18 months. The performance and physical specifications of these lasers including the their mechanical and thermal interface requirements were produced and subsequently used in the AEOLUS design and performance analyses.

The laser designs are based on Tm,Ho:YLF (Thulium, Holmium:YLF) lasing medium radiating at 2.06 microns wavelength. The lasers are pumped diode lasers at 785 nm wavelength. Two different architectures were used for these laser designs depending on the generated pulse energy.

The laser architectures are shown in figure 1. The Master Oscillator/Slave Laser (MO/SL) architecture was used for 25 mJ laser designs and Master Oscillator/Slave Laser/Power Amplifier (MO/SL/PA) architecture was used 200 mJ laser designs.
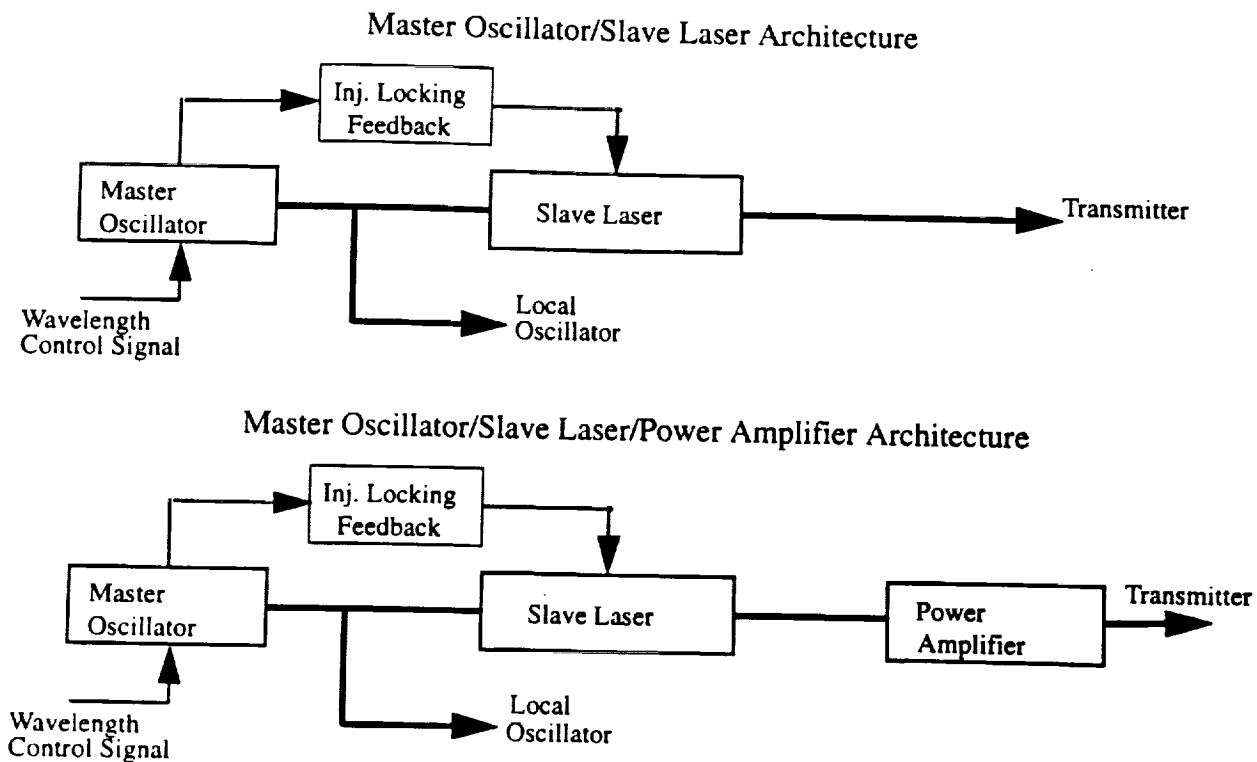
Master Oscillator/Slave Laser Architecture

Master Oscillator/Slave Laser/Power Amplifier Architecture

Figure 1. Solid State Laser Architectures for AEOLUS.

3.2   25 mJ LASER DESIGNS

A spaceborne coherent lidar transmitting 25 mJ pulses at 2.06 microns is capable of measuring cloud top and velocity and some clear air wind velocity measurements in high backscattering regions in the boundary layer. Two laser designs were developed for such measurements. Both lasers generate 25 mJ, 500 nsec pulses at 2.06 μm. One of the lasers is directly pumped by diode lasers and is capable of generating of up to 100 pulses per second. The other laser is pumped through fiber optic bundles and can generate 50 pulses per second. Figure 2 describes the design of the earlier laser. The slave laser uses a ring resonator configuration pumped by two diode laser arrays from both ends of the laser rod. Each diode laser array generates about 180 mJ per pulse. Two additional diode laser arrays are incorporated into the design as a contingency measure to reduce the risk of losing laser power during the mission. The backup diode lasers will be turned on if the power of the original diode lasers start to degrade or if one or both diodes fail to operate during the mission. The master oscillator uses a linear hemispherical resonator pumped by a 1 watt discrete diode laser. The master resonator uses a PZT driven tuning mechanism to provide a

tunable local oscillator for compensating the spacecraft induced Doppler frequency shift. Part of the master oscillator laser power is used as the local oscillator and the remained is used for injection-seeding of the slave laser.
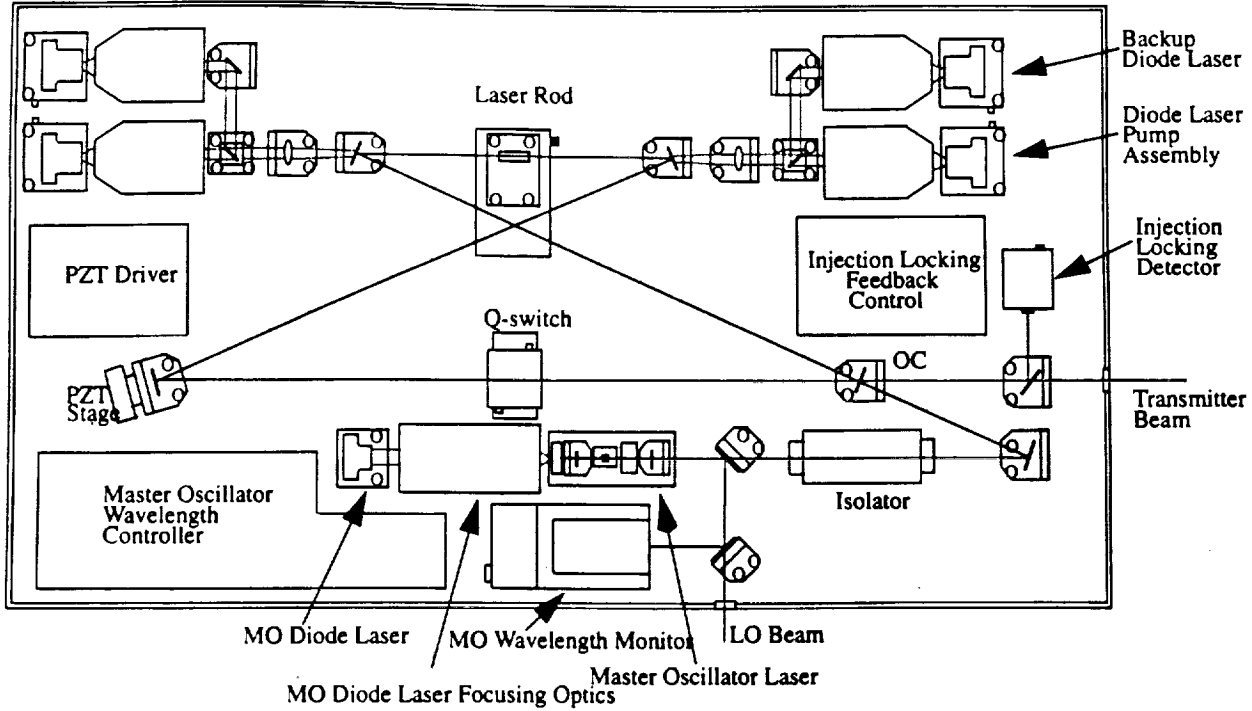

Figure 2. Direct Diode-Pumped, 25 mJ Solid State Laser Design.

Table 1 summarizes the laser performance and physical specifications and provides its power and thermal requirements. It should be noted that the laser power, mass and volume specifications include the laser thermal control and heat transfer unit. Although this laser is capable of operating at 100 Hz, the nominal repetition rate has been set at 15 Hz in order to meet the data rate and power requirements of a spacecraft that can be accommodated on a Pegasus class launch vehicle. The operating power of the laser increases almost linearly with the repetition rate, as shown in figure 3.

TABLE 1. Direct Diode-Pumped, 25 mJ Laser Specifications

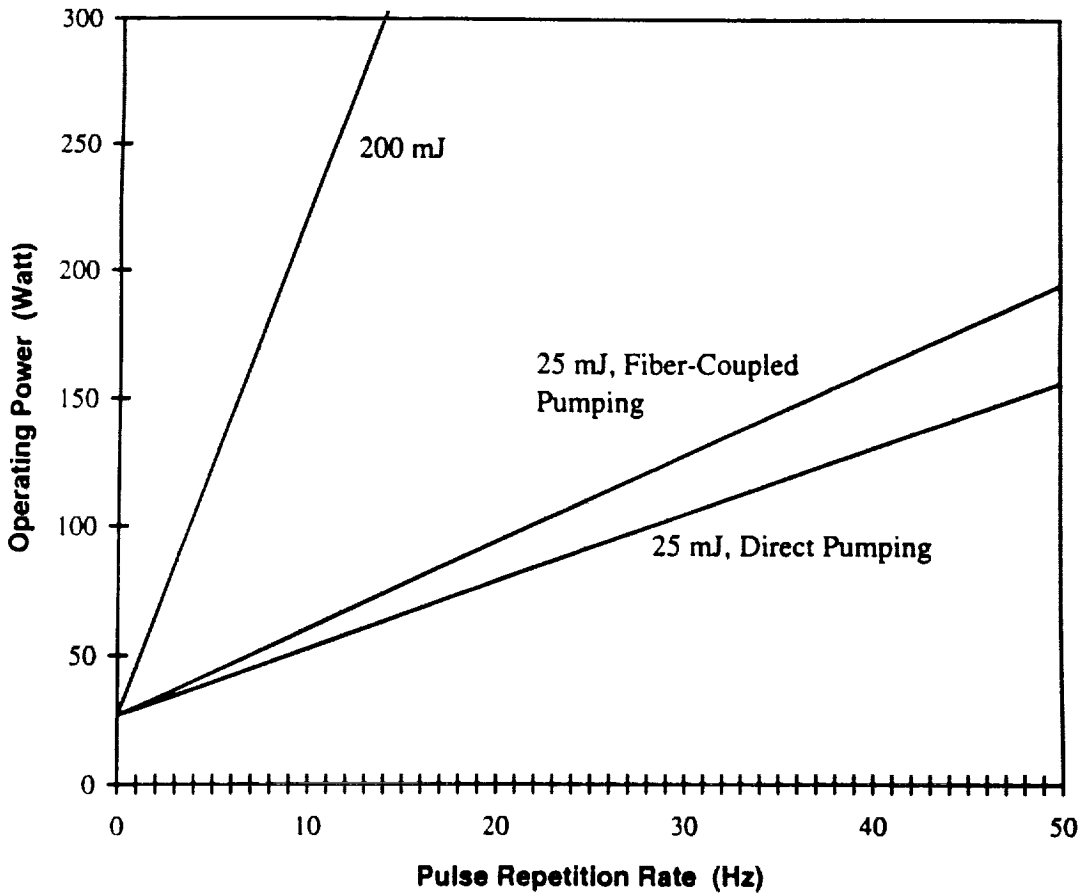|	
Pulse energy	25 mJ
Pulse width	500 nsec
Rep. rate	15 Hz
Life time	10^9 shots
Mission duration	116 days for 100% duty cycle
	1 year for 30% duty cycle
	6 years for 5% duty cycle
Operating power	66 watts
Standby power	8 watts
Dimensions	
Laser head	94X50X16 cm^3
Power supply	40X32X25 cm^3
Total volume	0.107 m^3
Weight	25 kg

Figure 3. Operating Power Vs. Pulse Repetition Rate for 25 mJ and 200 mJ Lasers.

For the fiber-coupled diode laser pumped laser, the diode lasers are removed from the slave laser head and their output energy is delivered through optical fiber bundles to the laser rod. This allows for an easier thermal management design, since the diodes are the main source of heat and at the same time require a stable operating temperature to within +/-1°C. Figure 4 describes this laser design concept. The slave laser still uses a ring resonator configuration and its rod is pumped from both ends. The master oscillator design is the same as previous designs which uses a linear hemispherical resonator pumped by a 1 watt discrete diode laser. The trade-off is additional diode laser power required to compensate for the losses in the optical fibers and to overcome the less uniform and lower concentration of the pump energy along the laser rod. The lower efficiency of the fiber-coupled diode pumped laser translates to about 11 Watts of additional operating power. This laser used two 200 mJ diode laser arrays as opposed to 180 mJ diode lasers used in the previous design. The specifications of this laser including its operating and standby powers, operating temperature range, physical dimensions and mass were estimated. These specifications are summarized in Table 2. The laser packaging design is illustrated in figure 5.

TABLE 2. Fiber-Coupled Diode Laser-Pumped, 25 mJ Laser Specifications

Pulse energy	25 mJ
Pulse width	500 nsec
Rep. rate	15 Hz
Life time	10^9 shots
Operating power	77 watts
Laser Head	15 watts
Laser Pump Module	38.5 watts
Power Supply	23.5 watts
Standby Power	8 watts
Laser Head	2 watts
Laser Pump Module	3 watts
Power Supply	3 watts
Operating Temperature	
Laser Head	5°C - 25°C
Laser Pump Module	5°C - 20°C
Power Supply	0°C - 40°C
Dimensions	
Laser head	80X40X16 cm^3
Laser Pump Module	35X25X20 cm^3
Power supply	40X25X20 cm^3
Total volume	0.09 m^3
Weight	22 kg

TOP VIEW

SLAVE LASER
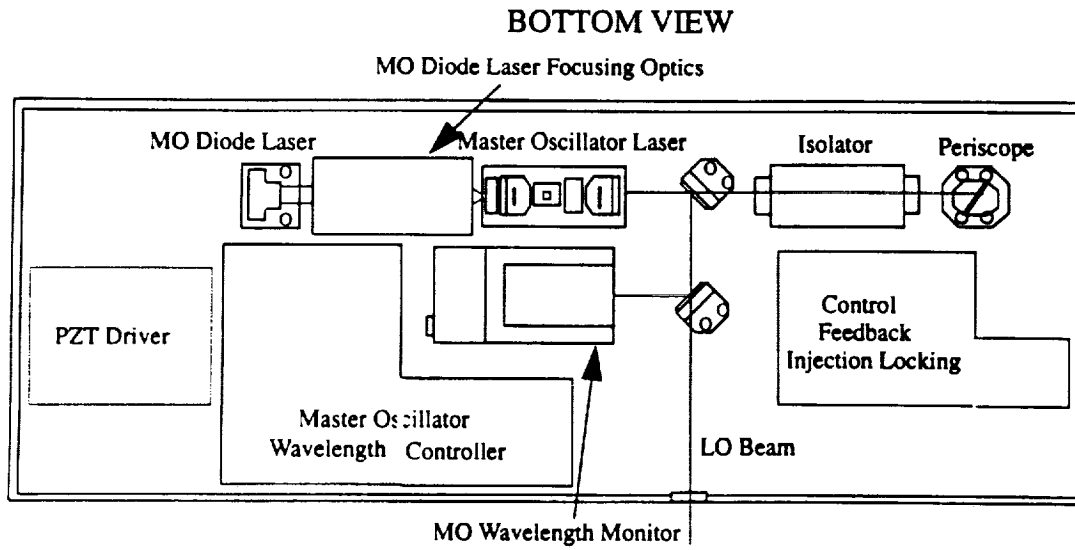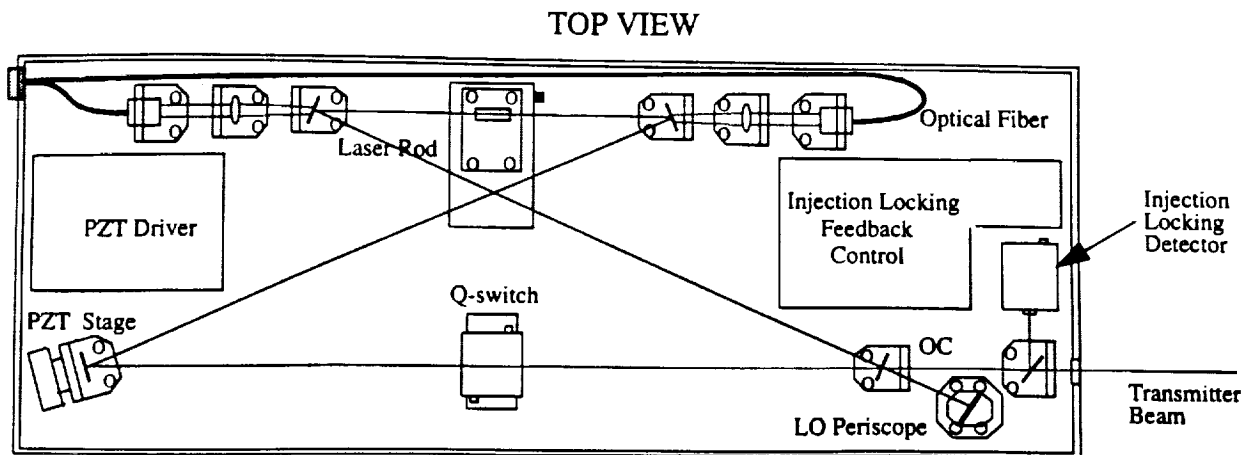
BOTTOM VIEW

MASTER OSCILLATOR LASER

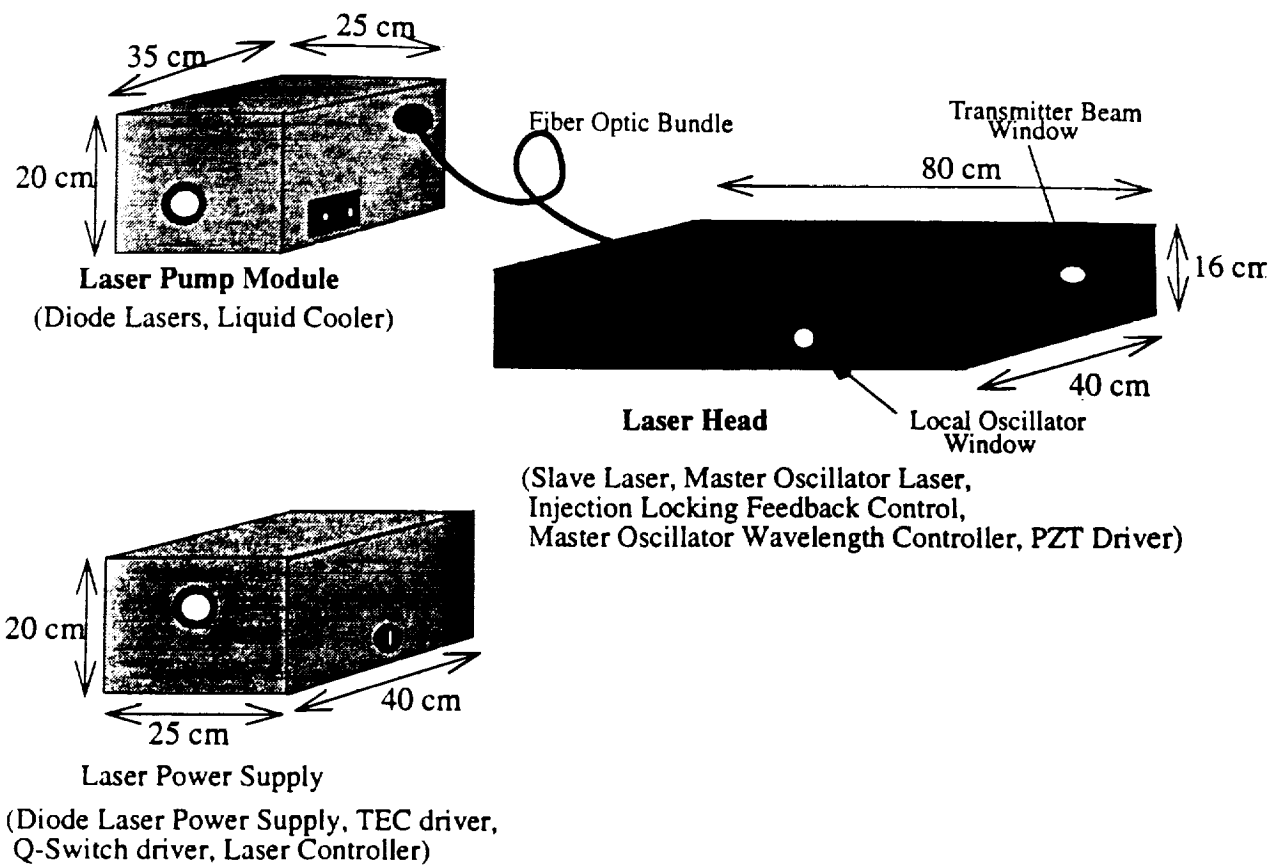Figure 4. Fiber-Coupled, Diode-Pumped, 25 mJ, Solid State Laser Design.

Figure 5. Packaging Design of the Fiber-Coupled, Diode-Pumped, 25 mJ Laser.

3.3 200 mJ LASER DESIGN

A 200 mJ, diode-pumped, Tm, Ho:YLF solid state laser design concept was developed utilizing the slave oscillator/power amplifier architecture. At 200 mJ pulse energy level, a spaceborne coherent lidar will be able to measure the wind fields in both continental and marine boundary layers and provide some measurements in the troposphere. Figure 6 describes the 200 mJ laser design. Part of the master oscillator laser power is used as the local oscillator and the remained is used to injection-seed a ring resonator, Q-switched, slave oscillator laser. The slave laser is end-pumped by two diode laser arrays, each generating 120 mJ, 400 μsec pulses. The slave oscillator laser generates 25 mJ at a single frequency. The laser pulsewidth is about 200nsec and the pulse repetition rate is 10 Hz. The slave oscillator laser output is then amplified by a single stage power amplifier to about 200 mJ. The power amplifier uses 12 diode arrays to pump a Tm, Ho:YLF rod from four sides. Each array generates 160 mJ of energy over the pulse duration of 400 μsec. Based on this design concept, the laser operating and standby powers, operating temperature range, physical dimensions and mass were estimated and used in the AEOLUS system design analyses. The packaging design and dimensions are shown in figure 7 and the overall performance and physical specifications are summarized in table 3.
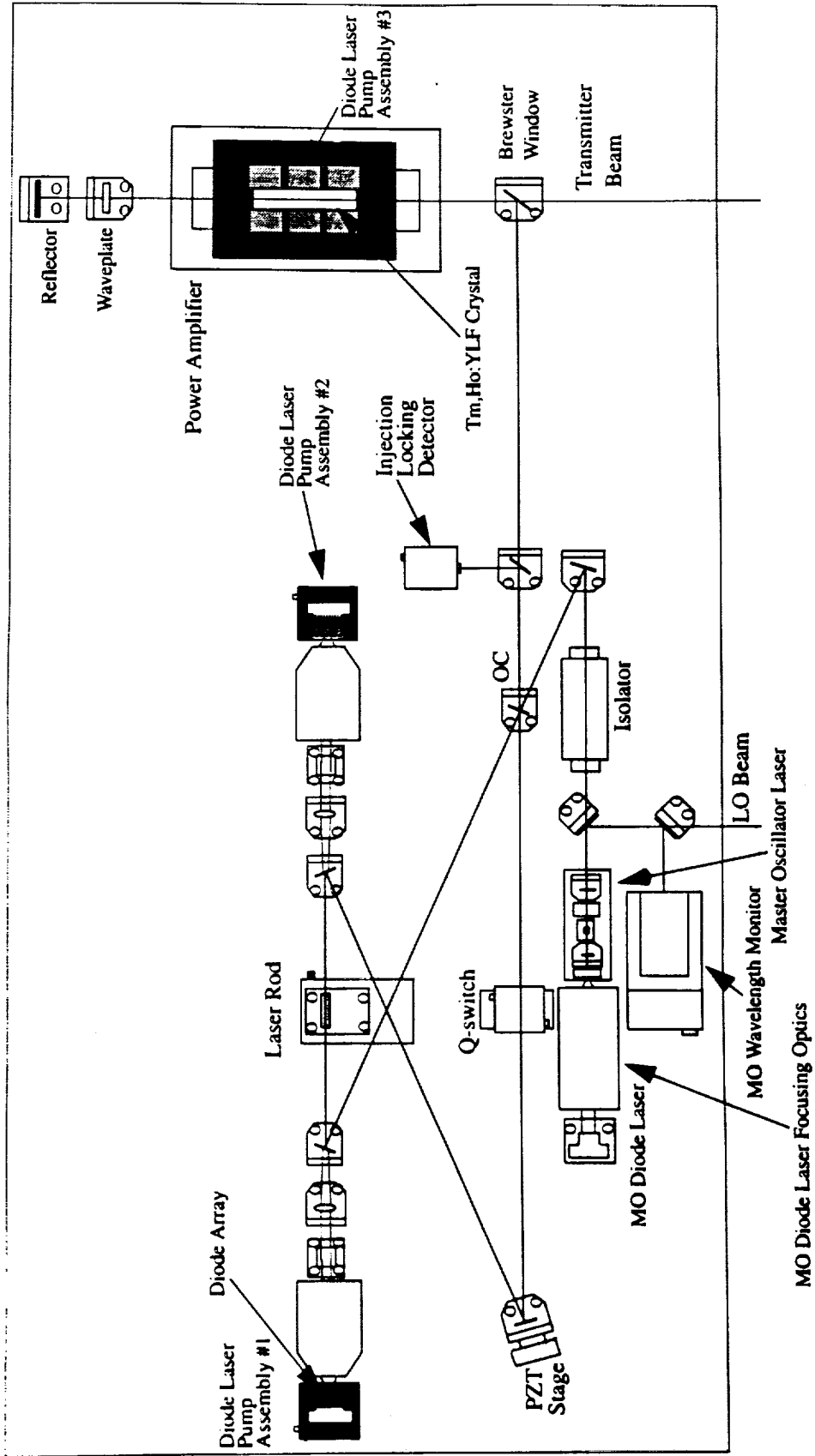
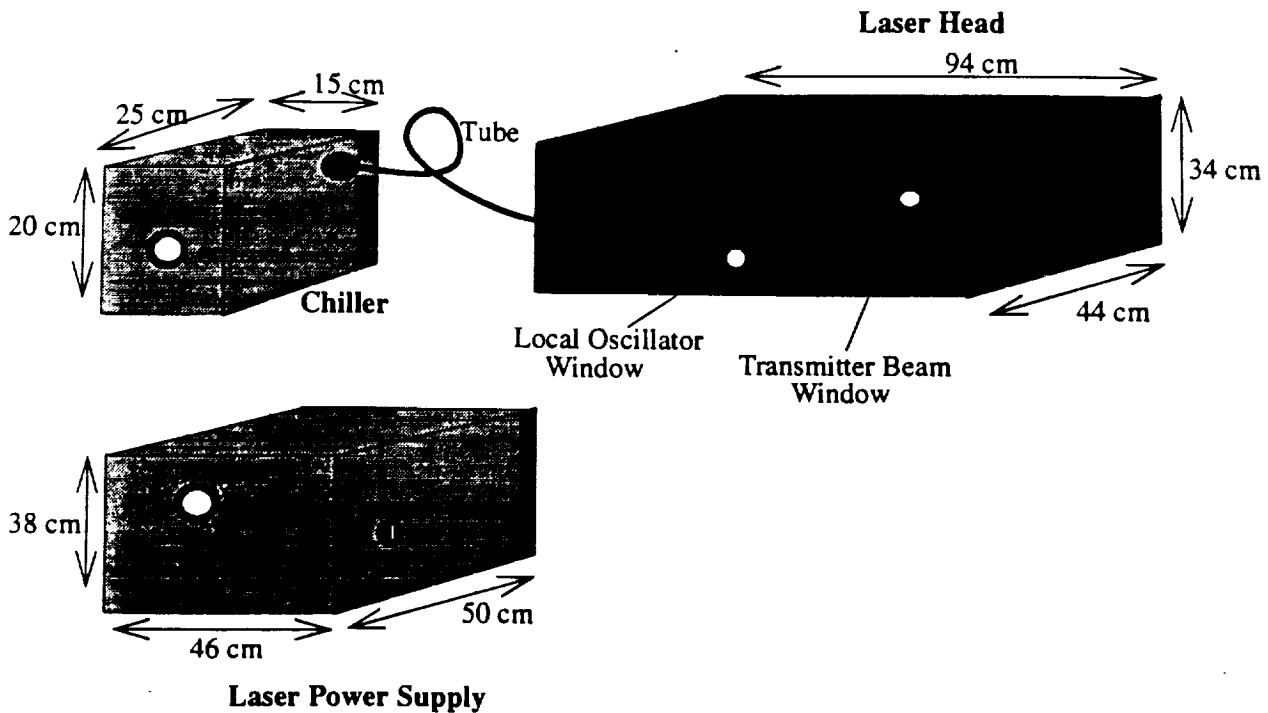Figure 6. 200 mJ, 10 Hz, Diode–Pumped Solid State Laser Design Concept.

Figure 7. Packaging Design of the 200 mJ Laser.

It should be noted that the MO/SL/PA architecture, used for this laser design, allows for scalability to higher pulse energies. This can be achieved by adding more amplifier stages and a phase conjugation device. The phase conjugator will be necessary to compensate for degradation of the beam quality, as more amplification stages are added and the pulse energy is increased to levels beyond several hundreds of millijoules. At these pulse energy levels, the thermal distortion and the stress-induced birefringence, caused by the pump intensity across the Tm,Ho:YLF rod in the amplifier, will degrade the beam spatial quality and the overall laser efficiency. The other limiting factors for increasing the laser pulse energy are the optical coating damage, thermal fracture, and thermal lensing. The optical coating damage threshold limits the pulse peak intensity along each amplifier rod. The thermal fracture limits the pump intensity across the amplifier rod and the pulse intensity along the rod. The thermal lensing, also caused by the pump intensity over the rod cross section, is a less serious problem than the thermal fracture and the coating damage and its effects on the laser performance can be minimized by a number of techniques. However, the thermal lensing of Tm,Ho:YLF crystals will probably prevent the laser to operate at a variable repetition rate. In the past, variable repetition rate has been considered for spaceborne coherent lidars in order to reduce the total instrument power consumption.

TABLE 3. Diode-Pumped, 200 mJ Laser Specifications

Pulse energy	200 mJ
Pulse width	200 nsec
Rep. rate	10 Hz
Life time	3×10^8 shots
Operating Power	223 watts
Laser Head	85 watts
Power Supply	47 watts
Chiller	91 watts
Warming-up Power (15 min)	117 watts
Laser Head	35 watts
Power Supply	47 watts
Chiller	35 watts
Standby Power	11 watts
Laser Head	3 watts
Power Supply	8 watts
Chiller	0 watts
Operating Temperature	
Laser Head	$5^{\circ}C$ - $25^{\circ}C$
Power Supply	$0^{\circ}C$ - $40^{\circ}C$
Dimensions	
Laser head	$94 \times 44 \times 34$ cm^3
Power Supply	$50 \times 46 \times 38$ cm^3
Chiller	$25 \times 20 \times 15$ cm^3
Total volume	0.236 m^3
Weight	34 kg

4.0 WIND VELOCITY MEASUREMENT ERROR
FOR A SCANNING PULSED COHERENT LIDAR

4.1 INTRODUCTION

Coherent lidars are capable of measuring the atmospheric wind velocity component along the transmitted beam. The vector wind velocity can then be measured by pointing the transmitted beam to at least three different directions. The most conventional method of directing the laser beam to different directions and measuring the atmospheric wind fields by a coherent lidar, either from a ground[14], or airborne[15,16], or a spaceborne platform[17-20], is the conically-scannig technique. This section describes the mathematical analysis perfomed under this contract for predicting the wind measurement accuracy using a connically-scanning, coherent lidar. Analytical expressions were derived for the error associated with the measurement of the horizontal wind velocity from a space-based platform. However, the analytical approach presented in this section can also be applied to the ground-based and airborne measurements of the atmospheric wind fields.

4.2 WIND MEASUREMENT ERROR OF A SPACEBORNE COHERENT LIDAR

The lidar measurement location and Line-Of-Sight (LOS) direction can be defined by vector r(t) in a cartesian coordinate system that is fixed with respect to the spacecraft (figure 1).

$$r(t) = r\sin\theta\cos\delta(t)\,\hat{x} + r\sin\theta\sin\delta(t)\,\hat{y} + r\cos\theta\hat{z} \qquad (1)$$

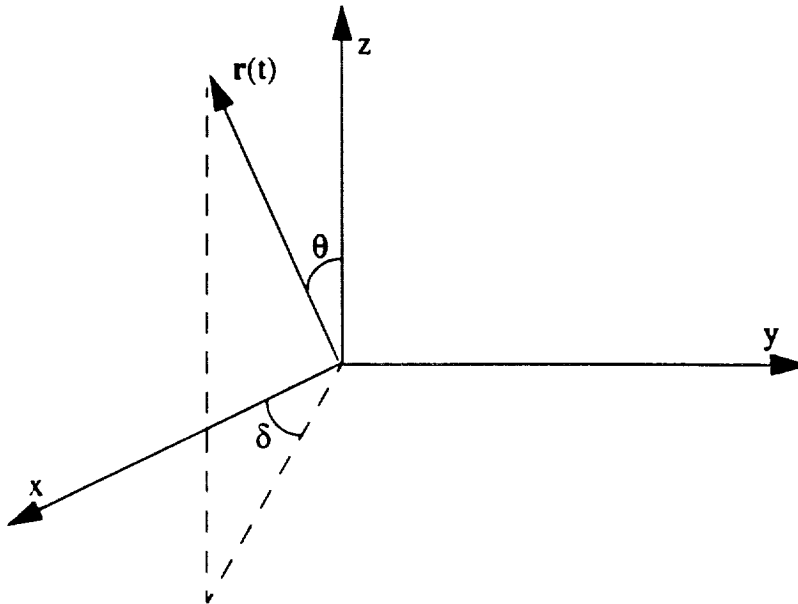Where θ and $\delta(t)$ are the lidar nadir and azimuth angles, respectively.

Figure 1. Line-Of-Site Vector r(t) in the spacecraft coordinate system.

The wind velocity at location **r** can be expressed in terms of three orthogonal components along the coordinate axes as

$$\mathbf{V}_a(\mathbf{r}, t) = u(\mathbf{r}, t)\,\hat{x} + v(\mathbf{r}, t)\,\hat{y} + w(\mathbf{r}, t)\,\hat{z} \tag{2}$$

The measured LOS Doppler velocity is then equal to

$$V_m(\mathbf{r}, t) = (\mathbf{V}_a + \mathbf{V}_s) \cdot (\mathbf{r}/r) = (u(\mathbf{r}, t) + u_s(\mathbf{r}, t))\sin\theta\cos\delta(t)$$
$$+ (v(\mathbf{r}, t) + v_s(\mathbf{r}, t))\sin\theta\sin\delta(t) + (w(\mathbf{r}, t) + w_s(\mathbf{r}, t))\cos\theta + \varepsilon_{sp}(\mathbf{r}, t) + \varepsilon(t) \tag{3}$$

where V_s is the spacecraft velocity with respect to the earth (i.e., it includes the effect of the earth rotation), $\varepsilon_{sp}(\mathbf{r}, t)$ is the velocity error due to the spacecraft pointing inaccuracy, and ε accounts for all the errors associated with the single-shot LOS velocity measurement that can result from the laser frequency jitter, atmospheric-induced spectral broadening, detector shot-noise and post detection electronic noise. Usually, the spacecraft and earth motion doppler velocities are subracted from the total Doppler velocity in the intitial stages of post detection processing, in order to extract the LOS wind velocity component. The measured LOS wind velocity can then be written as

$$V_D(\mathbf{r}, t) = (u(\mathbf{r}, t) + \Delta u_s(\mathbf{r}, t))\sin\theta\cos\delta(t) + (v(\mathbf{r}, t) + \Delta v_s(\mathbf{r}, t))\sin\theta\sin\delta(t)$$
$$+ (w(\mathbf{r}, t) + \Delta w_s(\mathbf{r}, t))\cos\theta + \varepsilon(t) + \varepsilon_{sp}(\mathbf{r}, t) \tag{4}$$

where the Δ terms are the inaccuracies or errors associated with the spacecraft velocity components provided by the on-board inertial and GPS instruments. By setting all the error terms equal to zero and using a pair of LOS Doppler velocities the horizontal wind velocity components can be derived

$$u_{ij} = u(q_{ij}, T_{ij}) = \frac{1}{\sin\theta\sin\delta_p(T_{ij})}\left[V_D(\mathbf{r}_j, t_j)\sin\delta(t_i) - V_D(\mathbf{r}_i, t_i)\sin\delta(t_j)\right] \tag{5}$$

$$v_{ij} = v(q_{ij}, T_{ij}) = \frac{1}{\sin\theta\sin\delta_p(T_{ij})}\left[V_D(\mathbf{r}_i, t_i)\cos\delta(t_j) - V_D(\mathbf{r}_j, t_j)\cos\delta(t_i)\right] \tag{6}$$

where

$$q_{ij} = \frac{\mathbf{r}_i + \mathbf{r}_j}{2}\ ,\quad T_{ij} = \frac{t_i + t_j}{2}\ \text{and}\ \delta_p(T_{ij}) = \delta(t_i) - \delta(t_j)$$

The average vertical wind velocity component has also been set equal to zero, since the vertical air currents have to cancel out over the measurement areas of tens of kilometers square being considered. The measured horizontal wind velocity components averaged over a measurement cell are then equal to

$$\hat{u} = \frac{1}{(N-1)^2 - \frac{(N-1)(N-2)}{2}} \frac{1}{\sin\theta} \sum_{i=1}^{N-1} \sum_{j=i+1}^{N} \frac{V_D(r_j, t_j) \sin\delta(t_i) - V_D(r_i, t_i) \sin\delta(t_j)}{\sin\delta_p(T_{ij})}$$

(7)

$$\hat{v} = \frac{1}{(N-1)^2 - \frac{(N-1)(N-2)}{2}} \frac{1}{\sin\theta} \sum_{i=1}^{N-1} \sum_{j=i+1}^{N} \frac{V_D(r_i, t_i) \cos\delta(t_j) - V_D(r_j, t_j) \cos\delta(t_i)}{\sin\delta_p(T_{ij})}$$

(8)

where N is the number of pulses within the measurement cell. The measured horizontal wind velocity magnitude and angle are given by

$$\hat{V}_H = \sqrt{\hat{u}^2 + \hat{v}^2} \qquad\qquad \hat{\alpha} = \text{atan} \frac{\hat{v}}{\hat{u}}$$

(9)

Using Taylor series expansion, Mean Square (MS) error associated with horizontal wind velocity magnitude and direction can be expressed in terms of the moments of $\hat{u}$ and $\hat{v}$. The Taylor series expansions of $\hat{V}_H$ about mean values of $\hat{u}$ and $\hat{v}$ is given by

$$\hat{V}_H = \sqrt{\langle\hat{u}\rangle^2 + \langle\hat{v}\rangle^2} + (\hat{u} - \langle\hat{u}\rangle)\frac{\partial\hat{V}_H}{\partial\hat{u}} + (\hat{v} - \langle\hat{v}\rangle)\frac{\partial\hat{V}_H}{\partial\hat{v}} + \frac{1}{2}\left((\hat{u} - \langle\hat{u}\rangle)^2 \frac{\partial^2\hat{V}_H}{\partial\hat{u}^2} + \right.$$
$$\left. 2(\hat{u} - \langle\hat{u}\rangle)(\hat{v} - \langle\hat{v}\rangle)\frac{\partial^2\hat{V}_H}{\partial\hat{u}\partial\hat{v}} + (\hat{v} - \langle\hat{v}\rangle)^2 \frac{\partial^2\hat{V}_H}{\partial\hat{v}^2} \right) + \dots$$

(10)

The Taylor series expansion of $\hat{\alpha}$ can be written in a similar fashion. Using Eq. (10) and neglecting the higher order terms, the MS errors for $\hat{V}_H$ and $\hat{\alpha}$ can be estimated as

$$\sigma^2_{V_H} = \langle\hat{V}_H^2\rangle - \langle\hat{V}_H\rangle^2 = \frac{\langle\hat{u}\rangle^2 \sigma^2_{\hat{u}} + 2\langle\hat{u}\rangle\langle\hat{v}\rangle R(\hat{u}, \hat{v}) + \langle\hat{v}\rangle^2 \sigma^2_{\hat{v}}}{\langle\hat{u}\rangle^2 + \langle\hat{v}\rangle^2}$$

(11)

$$\sigma^2_{\alpha} = \langle\hat{\alpha}^2\rangle - \langle\hat{\alpha}\rangle^2 = \frac{\langle\hat{v}\rangle^2 \sigma^2_{\hat{u}} - 2\langle\hat{u}\rangle\langle\hat{v}\rangle R(\hat{u}, \hat{v}) + \langle\hat{u}\rangle^2 \sigma^2_{\hat{v}}}{[\langle\hat{u}\rangle^2 + \langle\hat{v}\rangle^2]^2}$$

(12)

where $\sigma^2_{\hat{u}}$ and $\sigma^2_{\hat{v}}$ are the variances of the sample horizontal wind velocity components,

$R(\hat{u}, \hat{v})$ is their correlation function, and $\langle \hat{u} \rangle$ and $\langle \hat{v} \rangle$ are their means.

Using Eq. (7), the mean of the sample u component can be written as following

$$\langle \hat{u} \rangle = \frac{1}{(N-1)^2 - \frac{(N-1)(N-2)}{2}} \frac{1}{\sin\theta}$$

$$\sum_{i=1}^{N-1} \sum_{j=i+1}^{N} \frac{\langle V_D(r_j, t_j) \rangle \sin\delta(t_i) - \langle V_D(r_i, t_i) \rangle \sin\delta(t_j)}{\sin\delta_p(T_{ij})} \tag{13}$$

It can easily be shown that Eq. (13) reduces to $\langle \hat{u} \rangle = \bar{u}$, where $\bar{u}$ is the average wind velocity along x-direction over the measurement cell. The mean-square of the sample u is given by

$$\langle \hat{u}^2 \rangle = \left[\frac{1}{(N-1)^2 - \frac{(N-1)(N-2)}{2}} \right]^2 \frac{1}{\sin^2\theta} \sum_{i=1}^{N-1} \sum_{j=i+1}^{N} \sum_{k=1}^{N-1} \sum_{l=k+1}^{N} \frac{1}{\sin\delta_p(T_{ij}) \sin\delta_p(T_{kl})}$$

$$\left(\langle V_D(r_j, t_j) V_D(r_l, t_l) \rangle \sin\delta(t_i) \sin\delta(t_k) - \langle V_D(r_i, t_i) V_D(r_l, t_l) \rangle \sin\delta(t_j) \sin\delta(t_k) + \right.$$

$$\left. \langle V_D(r_i, t_i) V_D(r_k, t_k) \rangle \sin\delta(t_j) \sin\delta(t_l) - \langle V_D(r_j, t_j) V_D(r_k, t_k) \rangle \sin\delta(t_i) \sin\delta(t_l) \right) \tag{14}$$

Using Eqs. (13) and (14), variance of the sample u can be written as

$$\sigma^2_{\hat{u}} = \left[\frac{1}{(N-1)^2 - \frac{(N-1)(N-2)}{2}} \right]^2 \frac{1}{\sin^2\theta} \sum_{i=1}^{N-1} \sum_{j=i+1}^{N} \sum_{k=1}^{N-1} \sum_{l=k+1}^{N} \frac{1}{\sin\delta_p(T_{ij}) \sin\delta_p(T_{kl})}$$

$$(R_{jl} \sin\delta(t_i) \sin\delta(t_k) - R_{il} \sin\delta(t_j) \sin\delta(t_k) + R_{ik} \sin\delta(t_j) \sin\delta(t_l) - R_{jk} \sin\delta(t_i) \sin\delta(t_l)) \tag{15}$$

where R is the correlation between the measured LOS velocity pairs given by

$$R_{jl} = \langle (V_D(r_j, t_j) - \overline{V_D(r_j, t_j)}) (V_D(r_l, t_l) - \overline{V_D(r_l, t_l)}) \rangle =$$

$$\sin^2\theta [R(u(r_j, t_j), u(r_l, t_l)) \cos\delta(t_j) \cos\delta(t_l) + R(v(r_j, t_j), v(r_l, t_l)) \sin\delta(t_j) \sin\delta(t_l) +$$

$$R(u(r_j, t_j), v(r_l, t_l)) \cos\delta(t_j) \sin\delta(t_l) + R(v(r_j, t_j), u(r_l, t_l)) \sin\delta(t_j) \cos\delta(t_l)] +$$

$$\cos^2\theta R(w(r_j, t_j), w(r_l, t_l)) + E_\varepsilon + E_{sv} + E_{sp} \tag{16}$$

In this expresion, the cross-correlation between horizontal and vertical components of the wind velocity has been ignored for simplification reasons. The last three terms correspond to the errors resulting from the LOS measurement, the spacecraft and earth rotation velocities, and the spacecraft pointing inaccuracies, respectively. These quantities can be expressed in the following form:

$$E_\varepsilon = \begin{cases} \sigma_\varepsilon^2 & \text{for} \quad j = 1 \\ 0 & \text{for} \quad j \neq 1 \end{cases}$$

$$E_{sv} = \begin{cases} \sin^2\theta \, (\sigma_{u_s}^2 \cos^2\delta(t_j) + \sigma_{v_s}^2 \sin^2\delta(t_j)) + \cos^2\theta \sigma_{w_s}^2 & \text{for} \quad j = 1 \\ 0 & \text{for} \quad j \neq 1 \end{cases}$$

$$E_{sp} = \begin{cases} \sigma_{sp}^2 & \text{for} \quad j = 1 \\ 0 & \text{for} \quad j \neq 1 \end{cases} \tag{17}$$

where the cross-correlation between the three components of the spacecraft/earth rotation velocity has also been neglected for simplification reason. It is interseting to note that if the errors in the three components of the spacecraft velocity are identical, then E_{sv} is simply equal to σ_s^2, the variance of the spacefrat velocity.

The variance of the sample v and the correlation function of the samples u and v can be obtained similarly.

$$\sigma_{\hat{v}}^2 = \left[\frac{1}{(N-1)^2 - \dfrac{(N-1)(N-2)}{2}} \right]^2 \frac{1}{\sin^2\theta} \sum_{i=1}^{N-1} \sum_{j=i+1}^{N} \sum_{k=1}^{N-1} \sum_{l=k+1}^{N} \frac{1}{\sin\delta_p(T_{ij}) \sin\delta_p(T_{kl})}$$

$$(R_{jl}\cos\delta(t_i) \cos\delta(t_k) - R_{il}\cos\delta(t_j) \cos\delta(t_k) + R_{ik}\cos\delta(t_j) \cos\delta(t_l) - R_{jk}\cos\delta(t_i) \cos\delta(t_l)) \tag{18}$$

The correlation function $R(\hat{u}, \hat{v})$ is given by

$$R(\hat{u}, \hat{v}) = \langle (\hat{u} - \langle \hat{u} \rangle)(\hat{v} - \langle \hat{v} \rangle) \rangle$$

By substituting Eqs. (7) and (8) and using Eq. (13), the correlation function can be written as

$$R(\hat{u}, \hat{v}) = \left[\frac{1}{(N-1)^2 - \dfrac{(N-1)(N-2)}{2}} \right]^2 \frac{1}{\sin^2\theta} \sum_{i=1}^{N-1} \sum_{j=i+1}^{N} \sum_{k=1}^{N-1} \sum_{l=k+1}^{N} \frac{1}{\sin\delta_p(T_{ij}) \sin\delta_p(T_{kl})}$$

$$(R_{jk}\sin\delta(t_i) \cos\delta(t_l) - R_{ik}\sin\delta(t_j) \cos\delta(t_l) + R_{il}\sin\delta(t_j) \cos\delta(t_k) - R_{jl}\sin\delta(t_i) \cos\delta(t_k)) \tag{19}$$

Substituting Eqs. (15)-(19) in (11) and (12), the MS erors of the horizontal wind speed and direction due to the lidar LOS velocity errors, the spacecraft induced errors and the atmospheric effects can be obtained.

By observing Eqs. (15), (18) and (19), it can be seen that the velocity error is inversely propotional to $\sin\delta_p$. In other words, the velocity error decreases as the angle between the consecutive pulse pairs approaches +/-90° and approaches infinity as the angle between any pulse pair approach 0 or 180°. Therefore, it is necessary to either include a weighting function for averaging the pulse pairs for driving the horizontal wind velocity or simply ignore the pulse pairs for which the relative angle between them are smaller than a pre-determined threshold. The simplest weighting function for averaging the pulse pairs would be in the form of $\sin\delta_p$. Using $\sin\delta_p$ as the weighting function, Eqs. (15), (18) and (19) are modified to:

$$
\sigma_{\hat{u}}^2 = \left[\sum_{i=1}^{N-1} \sum_{j=k+1}^{N} \sin\delta_p (T_{ij}) \right]^{-2} \frac{1}{\sin^2\theta} \sum_{i=1}^{N-1} \sum_{j=i+1}^{N} \sum_{k=1}^{N-1} \sum_{l=k+1}^{N}
$$

$$
(R_{jl}\sin\delta(t_i)\sin\delta(t_k) - R_{il}\sin\delta(t_j)\sin\delta(t_k) + R_{ik}\sin\delta(t_j)\sin\delta(t_l) - R_{jk}\sin\delta(t_i)\sin\delta(t_l))
$$

$$(20)$$

$$
\sigma_{\hat{v}}^2 = \left[\sum_{i=1}^{N-1} \sum_{j=k+1}^{N} \sin\delta_p (T_{ij}) \right]^{-2} \frac{1}{\sin^2\theta} \sum_{i=1}^{N-1} \sum_{j=i+1}^{N} \sum_{k=1}^{N-1} \sum_{l=k+1}^{N}
$$

$$
(R_{jl}\cos\delta(t_i)\cos\delta(t_k) - R_{il}\cos\delta(t_j)\cos\delta(t_k) + R_{ik}\cos\delta(t_j)\cos\delta(t_l) - R_{jk}\cos\delta(t_i)\cos\delta(t_l))
$$

$$(21)$$

$$
R(\hat{u}, \hat{v}) = \left[\sum_{i=1}^{N-1} \sum_{j=k+1}^{N} \sin\delta_p (T_{ij}) \right]^{-2} \frac{1}{\sin^2\theta} \sum_{i=1}^{N-1} \sum_{j=i+1}^{N} \sum_{k=1}^{N-1} \sum_{l=k+1}^{N}
$$

$$
(R_{jk}\sin\delta(t_i)\cos\delta(t_l) - R_{ik}\sin\delta(t_j)\cos\delta(t_l) + R_{il}\sin\delta(t_j)\cos\delta(t_k) - R_{jl}\sin\delta(t_i)\cos\delta(t_k))
$$

$$(22)$$

Two Fortran computer programs were developed for numerical evaluation of horizontal wind velocity magnitude and direction defined by Eqs. (11) and (12) for different lidar and orbit parameters. One program uses Eqs. (20)-(22) to estimate the error for the $\sin\delta_p$ weighting function case, and the other program uses the Eqs. (15), (18), and (19) and an adjustable δ_p angle thershold routine that is described later in this section. Both programs use a shot pattern routine

that specifies the location and azimuth angle of each lidar pulse within any given measurement cell, and lidar and orbit parameters. The velocity error is then calculated using the equations specified above for given atmospheric parameters. Some of the results of these numerical analysis are represented in figures (2)-(7). For these results, a coherent lidar orbiting at 350 km altitude with 7.7 km/sec velocity has been used. The lidar pulse repetition rate and the scanning frequency have been set at 10 Hz and 10 RPM, respectively. It has also been assumed that the single shot LOS velocity measurement error (, due to the lidar and atmospheric turbulence,) σ_ϵ is equal to $0.4\sigma_H$, where σ_H is the standard deviation of the horizontal wind velocity over the measurement cell. The spacecraft velovity and pointing errors (E_{sv} and E_{sp}) are not included in the results of figures (2)-(7), in order to better illustrate the effects of the lidar LOS measurement errors and the atmospheric-induced errors on the horizontal wind estimation. The effect of the shot-to-shot atmospheric wind statistics on the horizontal wind estimation has been accounted for by using a gaussian correlation function of distance and time between the shots, as defined below.

$$R(u(r_1, t_1), u(r_2, t_2)) = \sigma_u^2 \exp\left(-\left(\frac{r_1 - r_2}{r_c}\right)^2\right) \exp\left(-\left(\frac{t_1 - t_2}{t_c}\right)^2\right) \tag{23}$$

Where r_c and t_c are the correlation distance and time. In figures (2)-(7), t_c has been assumed to be much longer than the measurement time for a 100 km^2 cell for which the last quantity of Eq. (23) is equal to 1. The same correlation function applies to the other two wind components. The correlation between the orthogonal components of the wind velocity (u,v) has been defined as

$$R(u(r_1, t_1), v(r_2, t_2)) = R_0\sigma_u\sigma_v \exp\left(-\left(\frac{r_1 - r_2}{r_c}\right)^2\right) \exp\left(-\left(\frac{t_1 - t_2}{t_c}\right)^2\right) \tag{24}$$

$$R(u(r_1, t_1), w(r_2, t_2)) = R(v(r_1, t_1), w(r_2, t_2)) = 0 \tag{25}$$

where R_0 is a constant less than unity. For the results presented here, R_0 has been assumed to be equal to 0.5.

For more rigrous analysis, Kolmogrov or Von Karman models may be used to define the statistics of the atmospheric winds[20-22]. However, these models apply to much smaller spatial scales than 100 km being considered here as the spatial resolution for the space-based measurements[23]. Therefore, the gaussian model of the atmospheric winds used for this analysis provide a reasonable prediction of the horizontal wind estimation accuracy over measurement cell of 100 km^2 and larger.

Figures (2) and (3) show the normalized RMS error of the horizontal wind velocity magnitude and direction for three different vertical wind variances as a function of the lidar scanning angle along nadir. The results shown in figures (2) and (3) have been obtained using the $\sin\delta_p$ weighting function for averaging all the pulse pair combinations. As can be seen from these figures, the

vertical wind variations over the measurement cell has a considerable effect on the accuracy of the horizontal wind estimation.
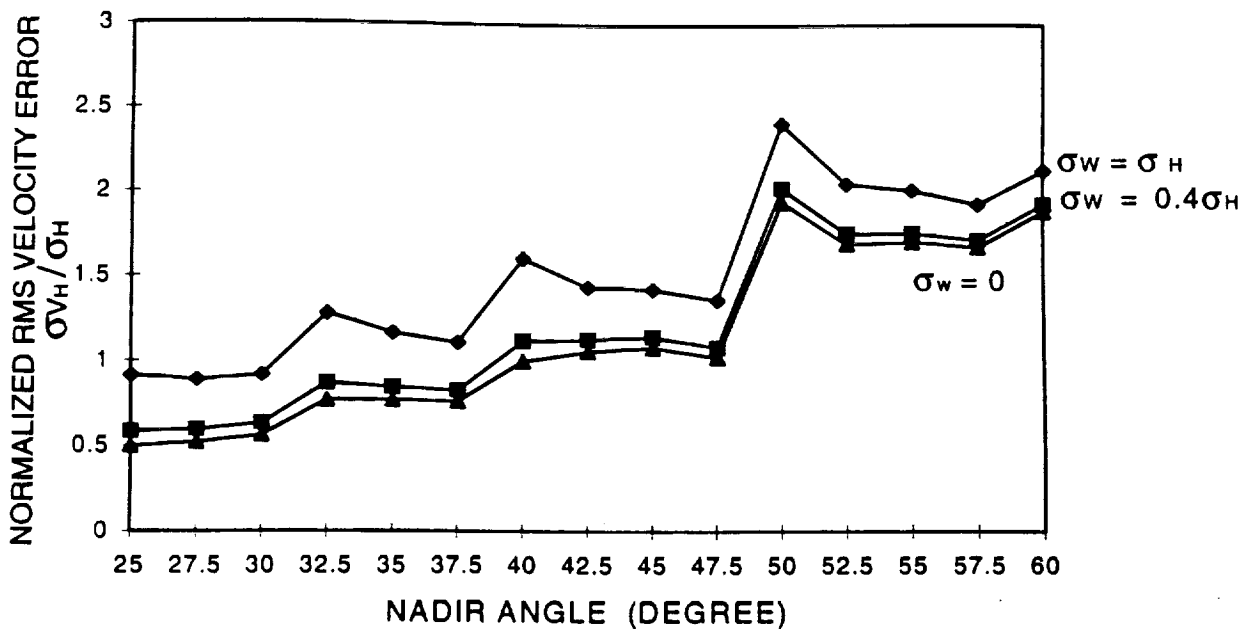

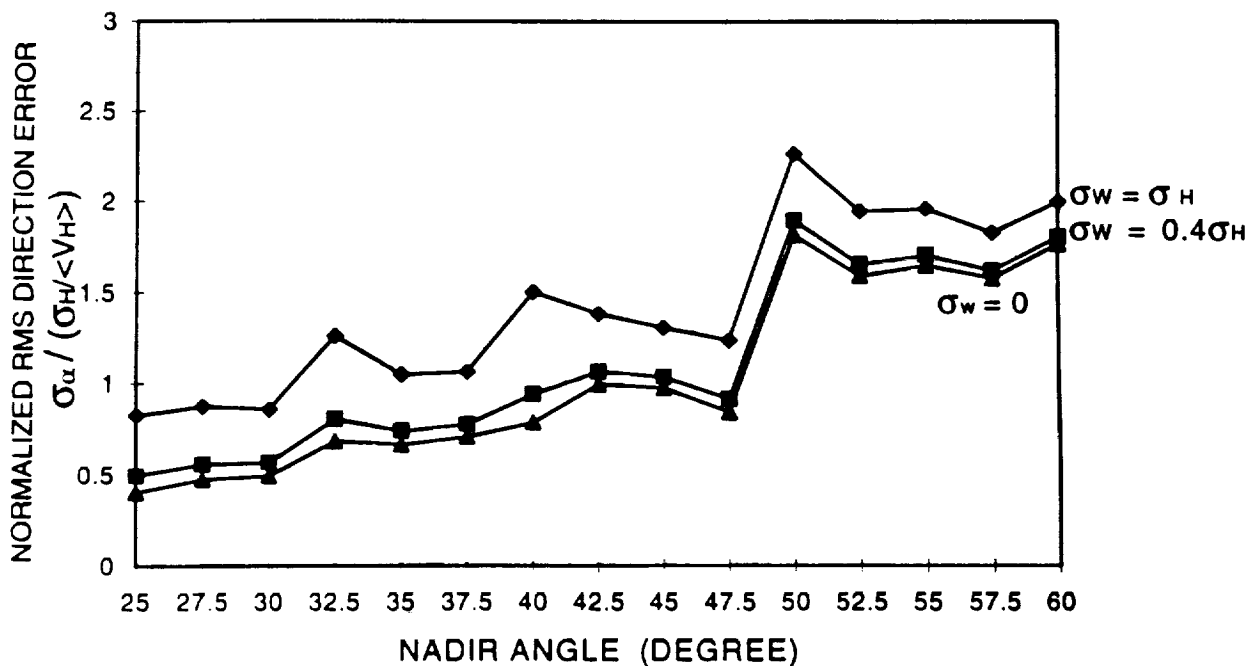Figure 2. Velocity magnitude error normalized by the standard deviation of the horizontal wind.

Figure 3. Wind direction error in radians normalized by the ratio of the standard deviation and the mean of the horizontal wind.

The measurement cell used for the results of figures (2) and (3) is shown in figure (4), where the lidar shots distribution is shown for 30° nadir angle. The nadir angle has two opposite effects on the horizontal wind estimation error. While the horizontal wind contribution to the LOS velocity increases with the nadir angle, resulting in smaller measurement error, the number of pulses in the measurement cells decreases with nadir angle which translates to larger error. These effects somewhat counter each other for nadir angles between 25 to 45 degrees as can be seen in figures (2) and (3). The number of lidar pulses and their pattern are obviously a function of the scanning frequency, the laser repetition rate as well as the nadir angle. Figure (5) shows the number of lidar pulses that are placed inside the measurement cell of figure (4) and the total number of pulse pair combinations used for estimating the average horizontal wind velocity.
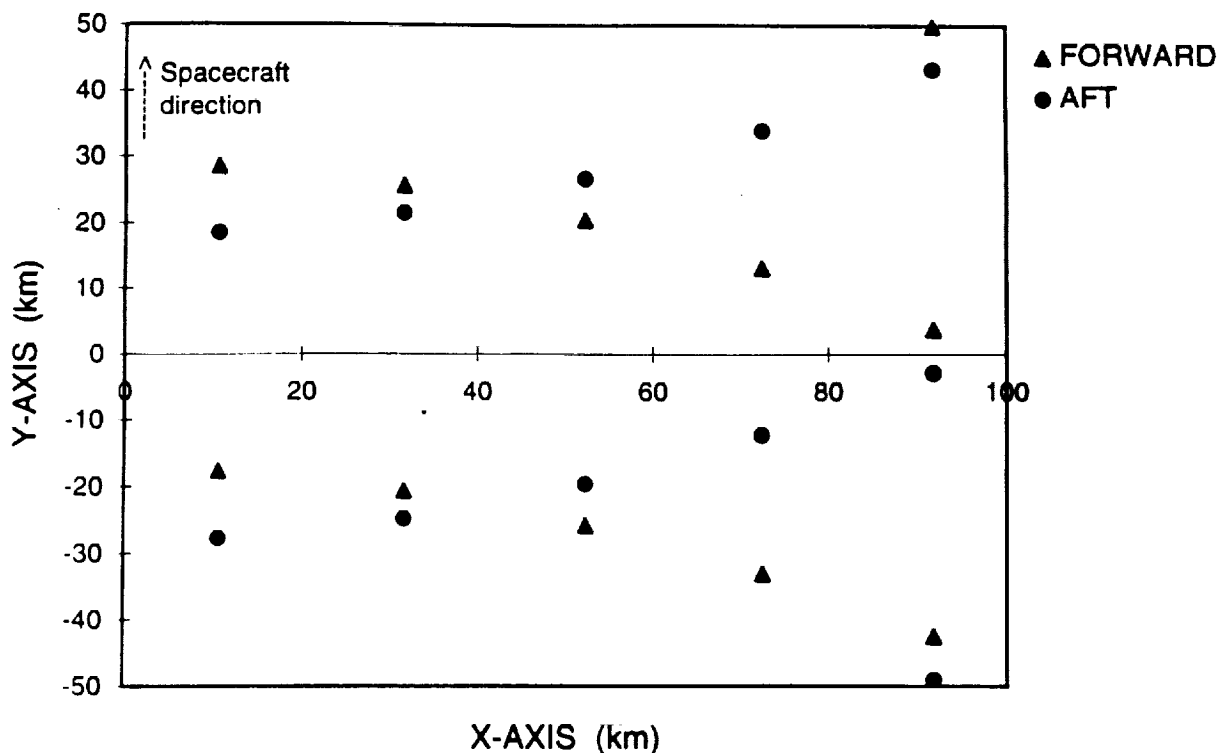

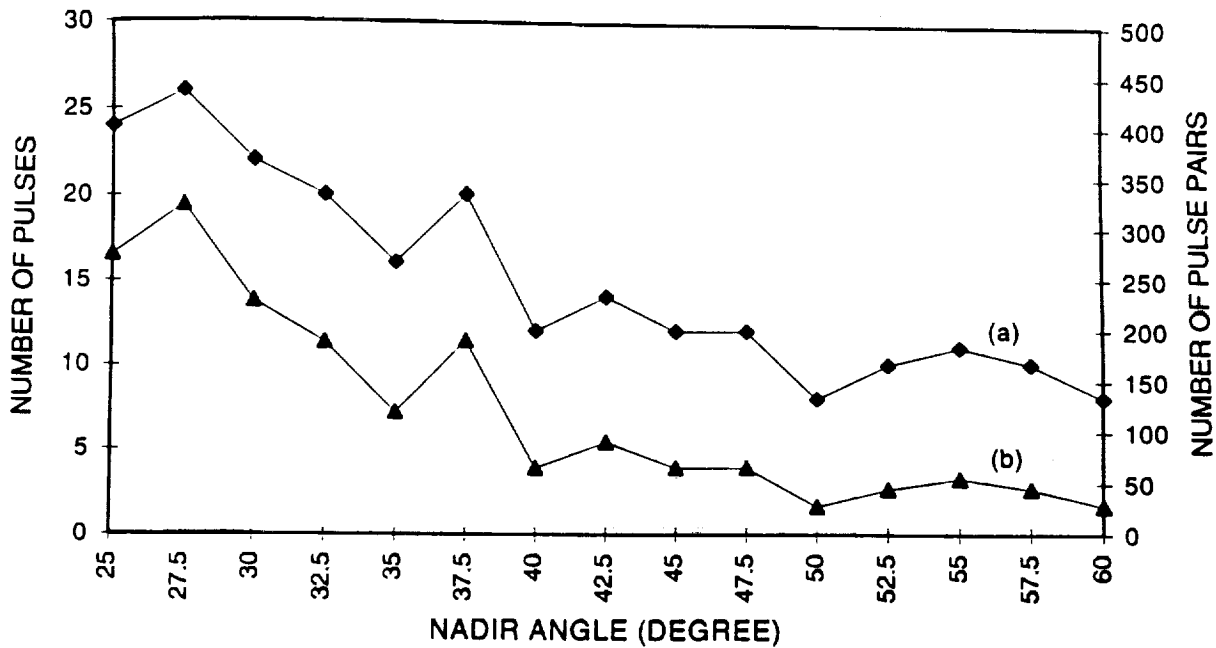Figure 4. The distribution of the lidar pulses for 30 degrees nadir angle.

Figure 5. The number of pulses and the total number of pulse pair combinations inside the 100 km^2 cell. (a) Number of pulses. (b) Number of pulse pairs.

The other technique used in this work and was briefly discussed earlier uses an adjustable angle threshold routine for which the optimum threshold angle δt for a given shot pattern is determined. Then, all the pulse pairs for having an azimuth angle difference $|\delta_p|$ or $|\delta_p - \pi|$ less than the threshold value are ignored and the remaining pulse pairs are averaged with equal weighting. Figure (6) compares the adjustable angle threshold algorithm with the $\sin \delta_p$ weighting function algorithm. Figure (7) shows the number of pulse pairs averaged for the angle threshold technique and the threshold angle as a function of nadir angle. In the same figure, the total number of possible pulse pairs is shown that illustrates the number of pulse pairs ignored by the threshold angle algorithm.
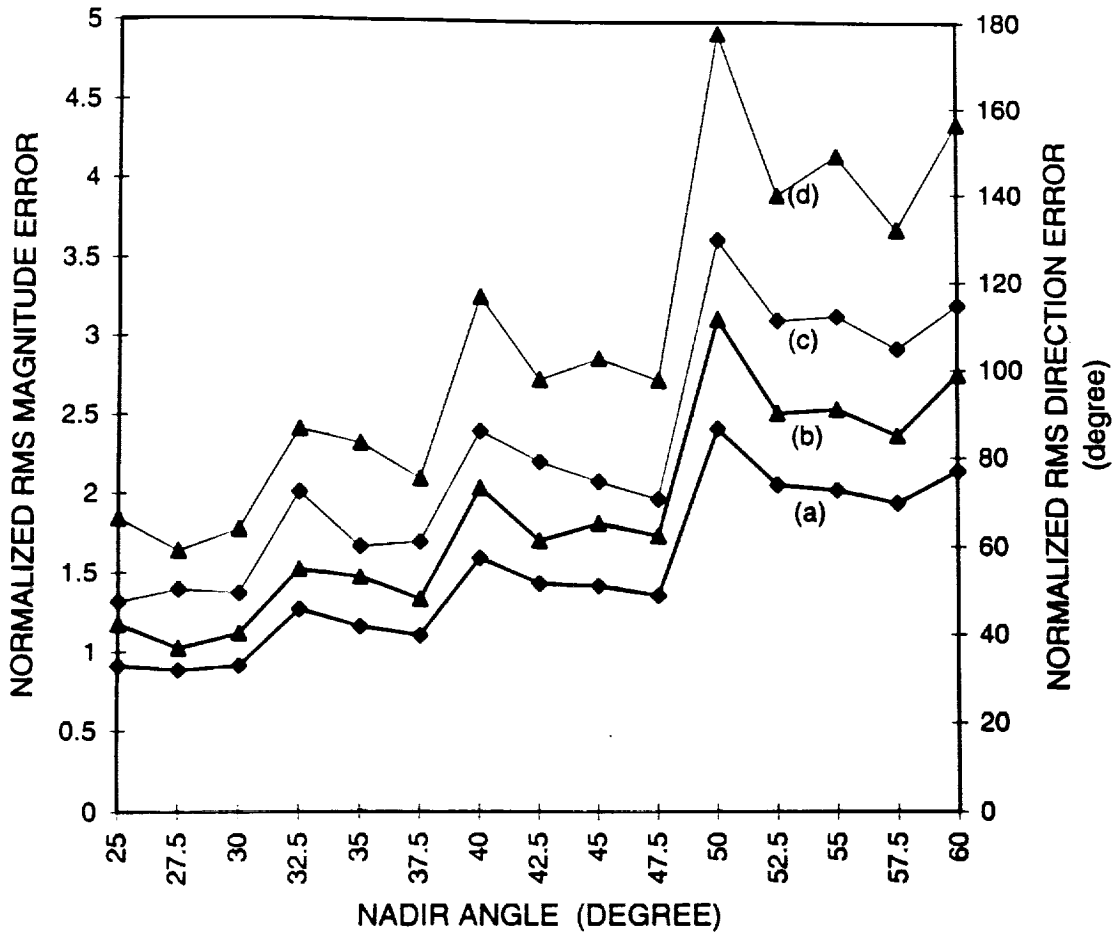
Figure 6. Comparison of the $\sin\delta_p$ weighting function and the angle threshold techniques for averaging the pulse pairs. RMS horizontal velocity magnitude and direction estimation errors normalized by σ_H and $\sigma_H/<V_H>$, respectively; for $\sigma_w=\sigma_H$, $\sigma_\varepsilon=0.4\sigma_H$ and $r_c=1$km. (a) Velocity magnitude error for $\sin\delta p$ weighting function technique. (b) Velocity magnitude error for angle threshold technique. (c) Velocity direction error for $\sin\delta p$ weighting function technique. (d) Velocity direction error for angle threshold technique.
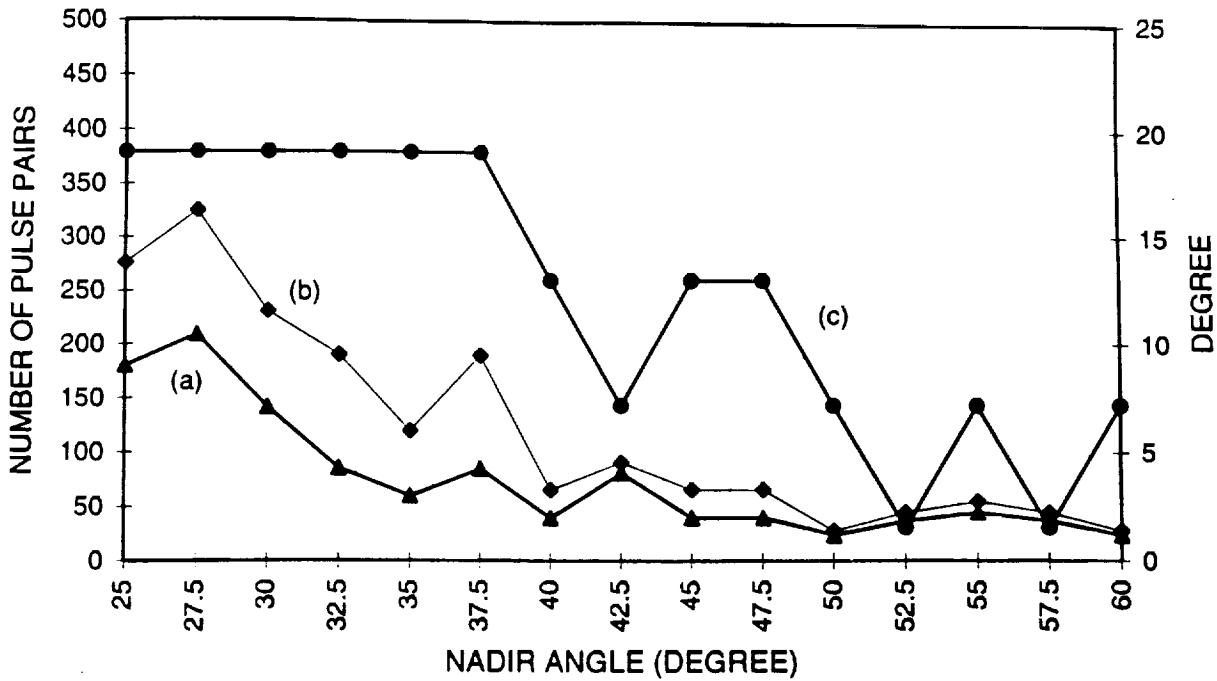
Figure 7. Number of pulse pairs used in the angle threshold routine and the corresponding threshold angle. (a) Number of pulse pairs used by the angle threshold technique. (b) The total number of pulse pairs combinations. (c) Threshold angle in degrees.

In previous work, a simple formulation has been obtained[25,26] which provides a rough estimate of the horizontal wind measurement error. This formulation for two extreme cases of dependent and independent LOS measurements can be expressed in the following form:

$$\sigma'^2_{indep} = \frac{\sigma^2_\varepsilon}{0.5N\sin^2\theta} + \frac{\sigma^2_H}{0.5N}$$

$$\sigma'^2_{dep} = \frac{\sigma^2_\varepsilon}{0.5N\sin^2\theta} + \frac{\sigma^2_H}{0.5} \tag{26}$$

where N is number of pulses in the measurement cell. σ'_{indep} applies to the case where the atmospheric winds at the footprints of the lidar pulses are uncorrelated, or in other words, all the individual LOS measurements within the measurement cell are independent of each other. σ'_{dep} applies to the other extreme for which all the LOS measurements within the cell are perfectly correlated. In figure 8, the expressions of Eq. (26) are compared with the results of the Eqs. (11), (20)-(22) for three different wind correlation distances of r_c=1km, 50km, 1nd 100km. Figure 8 shows that the simplified formulation underestimates the horizontal wind estimation error for both

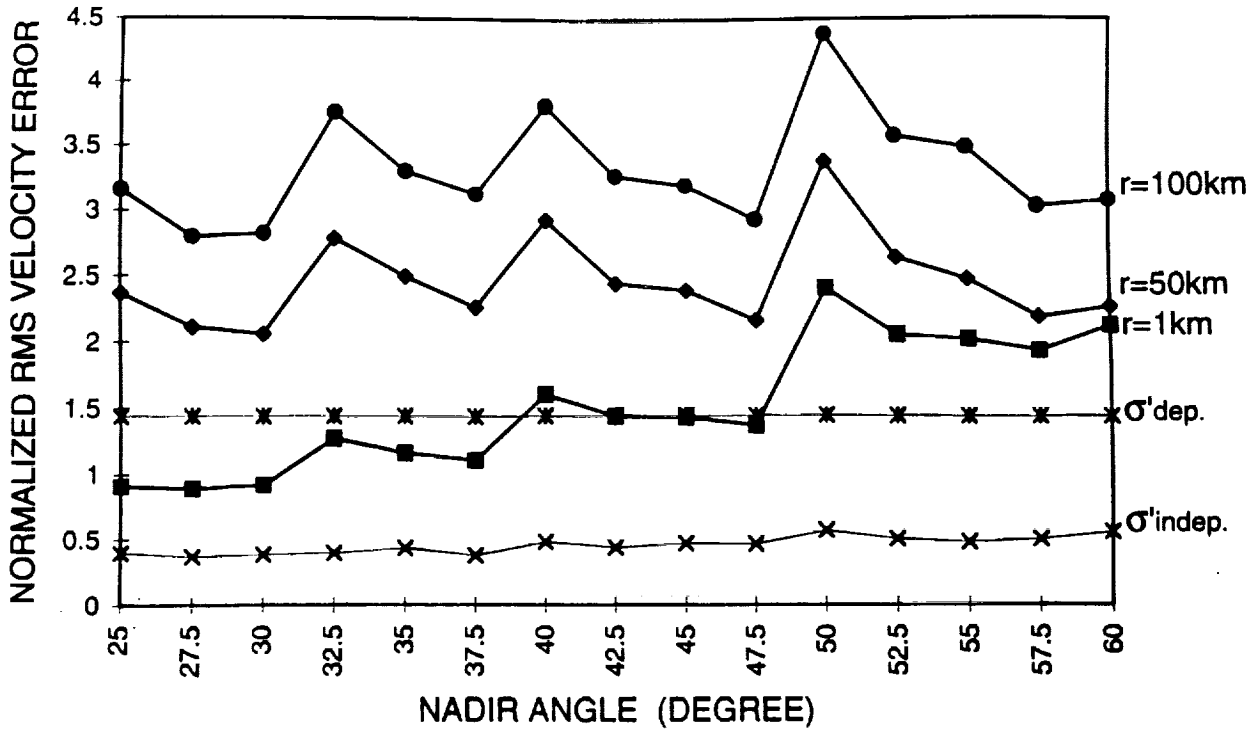cases. It can also be seen that the simplified expression have almost no dependence on the nadir angle.

Figure 8. Comparison of the results of Eq. (11) using $\sin\delta_p$ weighting function with the error expression in references [25 and 26].

The horizontal wind estimation error is highly dependent on the actual wind direction and the size and location of the measurement cell relative to the spacecraft flight path. All the results presented in figures (2)-(8) assume an actual horizontal wind velocity vector at 45° with respect to the X-axis (figure 1) and a $100km^2$ measurement cell shown in figure 4. The effect of the wind velocity direction on the horizontal wind estimation is illustrated in figure 9 which shows the normalized RMS wind velocity error for three different wind directions at 0°, 45° and 90°. The wind estimation error for a $150km^2$ measurement a cell (-75km<y<75km and 0<x<150km) is shown in figure 10. For comparison, the error associated with the $100km^2$ cell used for previous results is also shown.
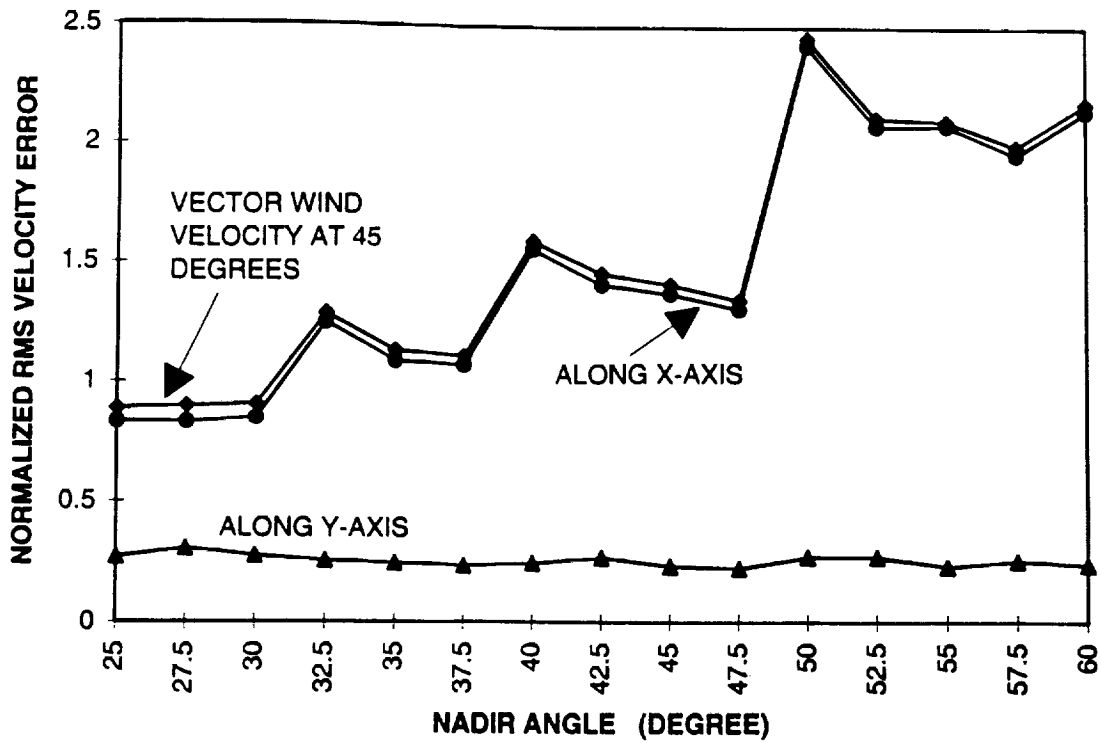
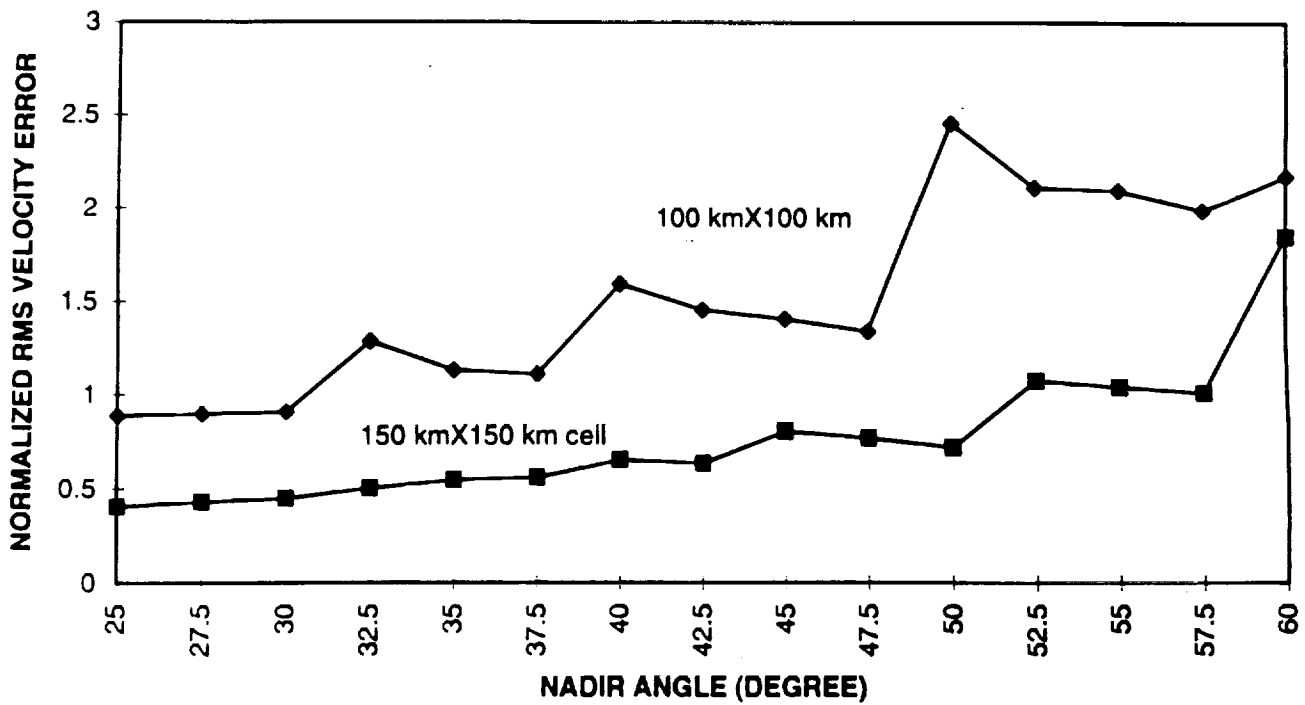Figure 9. Velocity estimation errors for three different wind directions.

Figure 10. Velocity estimation errors for 100 and 150 km^2 measurement cells.

4.3 SPECIAL CASE: WIND VELOCITY ESTIMATION ERROR FOR A PAIR OF PULSES

Assuming $\bar{u} = \bar{v}$ (i.e., vector wind velocity is at $45°$ angle) and neglecting the error in spacecraft/earth rotation velocity, the MS errors for the wind velocity and direction estimations for a pair of LOS measurements (N=2) can be written as

$$\sigma^2_{v_H} = \frac{1}{2\sin^2\theta \sin^2\delta_p(T_{12})}$$

$$(R_{11} + R_{22} - 2R_{12}\cos\delta_p(T_{12}) + 2R_{12}\sin(\delta(t_1) + \delta(t_2)) - R_{11}\sin 2\delta(t_2) - R_{22}\sin 2\delta(t_1))$$

$$(27)$$

$$\sigma^2_\alpha = \frac{1}{2\sin^2\theta \sin^2\delta_p(T_{12})}$$

$$(R_{11} + R_{22} - 2R_{12}\cos\delta_p(T_{12}) - 2R_{12}\sin(\delta(t_1) + \delta(t_2)) + R_{11}\sin 2\delta(t_2) + R_{22}\sin 2\delta(t_1))$$

$$(28)$$

Where Eqs. (15), (18) and (19) have been substituted in Eqs. (11) and (12). In general, the correlation between the wind velocity components is independent of absolute location and time of the measurements and is only a function of the distance and the time between the measurements. It can also be assumed without loss of generality that the statistics of the wind velocity along u and v directions are identical. Then the correlation function of Eq. (15) reduces to

$$R_{11} = R_{22} = \sin^2\theta\sigma_H^2 + \sin^2\theta\sin 2\delta(t_1)R(u(r_1,t_1),v(r_1,t_1)) + \cos^2\theta\sigma_w^2 + \sigma_\varepsilon^2 \quad (29)$$

and

$$R_{12} = \sin^2\theta[R(u(r_1,t_1),u(r_2,t_2))\cos\delta_p(T_{12}) + R(u(r_1,t_1),v(r_2,t_2))\sin(\delta(t_1) + \delta(t_2))]$$
$$+ \cos^2\theta R(w(r_1,t_1),w(r_2,t_2))$$

$$(30)$$

where

$$\sigma_H^2 = \sigma_u^2 = \sigma_v^2$$

$$R(u(r_1,t_1),u(r_2,t_2)) = R(v(r_1,t_1),v(r_2,t_2))$$

$$R(u(r_1,t_1),v(r_2,t_2)) = R(v(r_1,t_1),u(r_2,t_2))$$

The MS error associated with the LOS measurements has also been assumed to be independent from shot to shot which is the case for most practical situations. As an example, let us assume that the wind velocities at (r_1,t_1) and (r_2,t_2) are completely independent and the u and v components are uncorrelated. In this case

$$R_{11} = R_{22} = \sigma^2_{atm} + \sigma^2_\varepsilon \qquad and \qquad R_{12} = 0$$

where $\sigma^2_{atm} = \sigma^2_H = \sigma^2_w$. Eqs. (27) and (28) then reduce to

$$\sigma^2_{V_H} = \frac{\sigma^2_{atm} + \sigma^2_\varepsilon}{\sin^2\theta \sin^2\delta_p (T_{12})} \left(1 - \frac{\sin 2\delta(t_1) + \sin 2\delta(t_2)}{2} \right) \tag{31}$$

$$\sigma^2_\alpha = \frac{1}{\sin^2\theta \sin^2\delta_p (T_{12})} \left(1 + \frac{\sin 2\delta(t_1) + \sin 2\delta(t_2)}{2} \right) \tag{32}$$

When the LOS vectors projected in the horizontal plane are orthogonal to each other, Eqs. (31) and (32) reduce to the familiar expression

$$\sigma^2_{V_H} = \sigma^2_\alpha = \frac{\sigma^2_{atm} + \sigma^2_\varepsilon}{\sin^2\theta} \tag{33}$$

This expression is identical to Eq. (26), the error expression for independent pulses from reference [25]. Let us now assume that the wind velocities are perfectly correlated and their u and v components are independent of each other. In this case

$$R_{11} = R_{22} = \sigma^2_{atm} + \sigma^2_\varepsilon$$

$$R_{12} = \sin^2\theta \cos\delta_p (T_{12}) \sigma^2_{atm} + \cos^2\theta \sigma^2_{atm}$$

Substituting in Eqs. (27) and (28)

$$\sigma^2_{V_H}, \sigma^2_\alpha = \frac{\sigma^2_{atm} + \sigma^2_\varepsilon}{\sin^2\theta \sin^2\delta_p (T_{12})} \left(1 \pm \frac{\sin 2\delta(t_1) + \sin 2\delta(t_2)}{2} \right) - $$
$$\frac{\sin^2\theta \cos\delta_p (T_{12}) \sigma^2_{atm} + \cos^2\theta \sigma^2_{atm}}{\sin^2\theta \sin^2\delta_p (T_{12})} (\cos\delta_p (T_{12}) \mp \sin(\delta(t_1) + \delta(t_2))) \tag{34}$$

When the LOS vectors projected in the horizontal plane are orthogonal to each other, Eq. (34) reduces to

$$\sigma^2_{V_H} = \frac{(1 + \cos^2\theta \cos 2\delta(t_1)) \sigma^2_{atm} + \sigma^2_\varepsilon}{\sin^2\theta} \tag{35}$$

$$\sigma^2_\alpha = \frac{(1 - \cos^2\theta \cos 2\delta(t_1)) \, \sigma^2_{atm} + \sigma^2_\varepsilon}{\sin^2\theta} \qquad (36)$$

For $\delta(t_1) = 45^o$, the expressions above will become identical to Eq. (33) and for $\delta(t_1) = 0, 180^o$, it reduces to

$$\sigma^2_{v_H} = \frac{(1 + \cos^2\theta) \, \sigma^2_{atm} + \sigma^2_\varepsilon}{\sin^2\theta}$$

$$\sigma^2_\alpha = \sigma^2_{atm} + \frac{\sigma^2_\varepsilon}{\sin^2\theta}$$

For $\delta(t_1) = 90^o or 270^o$, Eqs. (35) and (36) are equal to

$$\sigma^2_{v_H} = \sigma^2_{atm} + \frac{\sigma^2_\varepsilon}{\sin^2\theta}$$

$$\sigma^2_\alpha = \frac{(1 + \cos^2\theta) \, \sigma^2_{atm} + \sigma^2_\varepsilon}{\sin^2\theta}$$

5.0 RELATED ACTIVITIES

5.1 LIDAR COMPUTER DATABASE

A computer database of lidar related materials was designed and developed to serve as a source of information for lidar research and development. This database uses Paradox software with a menu type design that allows a number of options for searching through the database and presenting the selected items. A database user interface was designed and implemented, and a number of "help" files were written that allows the database to be used without any prior knowledge of the Paradox software. Over 1350 items were entered into this database which include about 950 journal papers, 350 reports and technical memorandums, and 50 books, thesis and proposals. The database entries cover areas related to the theory, development, testing, and operation of lidar components and systems, and the atmosphere optical properties. This database include all the lidar related materials at NASA/MSFC Electro-Optical Branch, which were identified and indexed by the UAH personnel. Both the database and the users interface software have been made available to the scientific community.

To further improve the data entry process and sustaining the database up to date, an automated data entry system was designed to be incorporated in the future. This data entry system will use a page scanner hardware and an Optical Character Recognition (OCR) software. In addition a World Wide Web (WWW) interface for the database was designed to be implemented in the future. This database WWW interface will allow the industry, academic, and the government agencies and laboratories to access the database through computer networks.

5.2 NASA SENSOR WORKING GROUP MEETINGS

UAH personnel attended two Sensor Working Group Meetings at NASA Langley Research Center (May 3-5, 1994) and NASA Goddard Space Flight Center (September 21-22, 1994). The results of the "analyses of measurements for solid state laser remote lidar sensing" performed the UAH personnel were presented at these meetings. The status of the Detector Characterization Facility development, and the design and capabilities of the companion Laser Characterization Facility developed earlier at the NASA/MSFC were also described at these meetings. In order to further assess the NASA Laser Remote Sensing Program and the technical direction being pursued under this program, UAH acquired the services of two of the leaders in field to participate in the earlier meeting and to provide appropriate recommendations. These scientists were Professor Martin Stickley of University of Central Florida and Dr. T.Y. Fan of MIT Lincoln Laboratory.

In addition to the NASA Sensor Working Group Meetings, a number of other meetings were attended by the UAH personnel and the work being performed under this contract was described. These meetings include the "NASA 2-micron Solid State Laser Technology Review" in washington, D.C., November 8-9, 1993; "Meeting of NOAA Working Group on Space-Based Lidar Winds" in Huntsville, Alabama, July 12-14, 1994; and the "NASA Solid State Coherent Doppler Lidar Program Coordination and Review Meetings" at Jet Propulsion Laboratory, November 16, 1993, NASA/LaRC, July 18-19, 1994.

REFERENCES

1. D.L. Spears and R.H. Kingston, "Anomalous noise behavior in wide-bandwidth photodiodes in heterodyne and background-limited operation," Appl. Phys. Lett. 34, May 1979.

2. R. G. Frehlich and M. J. Kavaya, "Coherent laser radar performance for general atmospheric refractive turbulence," Appl. 30, December 1991

3. R.T. Ku and D.L. Spears, "High-sensitivity infrared heterodyne radiometer using a tunable-diode-laser local oscillator," Opt. Lett. 1, September 1977.

4. R. G. Frehlich, "Estimation of the nonlinearity of a photodetector," Appl. Opt. 31, October 1992.

5. J. F. Holmes and B. J. Rask, "Optimum optical local-oscillator power levels for coherent detection with photodiodes," Appl. Opt. 34, February 1995

6. J. M. Hunt, J. F. Holmes, and F. amzajerdian, "Optimum local oscillator levels for coherent detection using photoconductors," Appl. Opt. 27, August 1988

7. M.J. Post and R.E. Cupp, "Optimizing a pulsed Doppler lidar," Appl. Opt. 29, October 1990.

8. H. van de Stadt, "Heterodyne detection at a wavelength of 3.39 μm for astronomical purposes," Astron. and Astrophys. 36, 341-348, 1974.

9. J. Gay, A. Journet, B. Christophe, and M. Robert, "Heterodyne detection of blackbody radiation," Appl. Phys. Lett. 22, May 1973.

10. D. L. Spears, "Long-wavelength photodiode development," NASA report no. NAS-5-25717, August 1983

11. T. G. Blaney, "Signal-to-noise ratio and other characteristics of heterodyne radiation receivers," Space Science Reviews 17, 1975

12. R.H. Kingston, "Detection of optical and infrared radiation," Springer Series in Optical Sciences, V. 10, 1979.

13. M.J. Kavaya, G.D. Spiers, E.S. Lobl, J. Rothermel, and V.W. Keller, "Direct global measurements of tropospheric winds employing a simplified coherent laser radar using fully scalable technology and technique," Proc. Of SPIE International Symposium on Optical Engineering in Aerospace Sensing, Technical Conference on Space Instrumentation and Dual-Use Technologies, 2214-31, Apr 6, 1994.

14. J.G. Hawley, R. Targ, S.W. Henderson, C.P. Hale, M.J. Kavaya, and D. Moerder, "Coherent launch-site atmospheric wind sounder: theory and experiment" Appl. Opt. 32, August 1993.

15. J. W. Bilbro, C. DiMarzio, D. Fitzjarrald, S. Johnson, and W. Jones, "Airborne Doppler lidar measurements" Appl. Opt. 25, November 1986.

16. R.J. Keeler, R.J. Serafin, R.L. Schwiesow, D.H. Lenschow, J.M. Vaughn, and A.A. Woodfield, "An airborne laser air motion sensing system, Part I: Concept and preliminary experiment," J. Atm and Oceanic Tech. 4, 1987.

17. R.T. Menzies, "Doppler lidar atmospheric wind sensor: a comparative performance evaluations for global measurement applications from earth orbit," Appl. Opt. 25, August 1986.

18. R.G. Beranek, J.W. Bilbro, D.E. Fitzjarrald, W.D. Jones, V.W. Keller, B.S. Perrine, "Laser Atmospheric Wind Sounder (LAWS)," SPIE v. 1062, Laser Applications in Meteorology and Earth and Atmospheric Remote Sensing, 1989.

19. W.E. Jones, D.J. Wilson, W.W. Montgomery, C. Robert, S.C. Kurzius, S. Ghoshroy, R.E. Joyce, C. Buczek, Z.S. Karu, G.R. Power, "Final Report: Laser Atmospheric Wind Sounder(LAWS) Phaser II," NASA Contract No. NAS8-37590, Lockheed, Report No., June 1992.

20. "Definition and Preliminary Design of the LAWS (Laser Atmospheric Wind Sounder) Phase II Final Report Volume II," NASA Contract No. NAS8-37589, GE Astro Space Division, September 1992.

21. V.I. Tatarskii, "The effect of the turbulent atmosphere on wave propagation," Springfield, Va., U.S. Dept. of Commerce, 1971.

22. L. Kristensen and D.H. Lenschow, "The spectral velocity tensor for homogeneous boundary-layer turbulence," Boundary-Layer Meteorology 47, 149-193, Kluwer Academic Publishers, Netherlands, 1989.

23. L. Kristensen and J.E. Gaynor, "Errors in second moments estimated from monostatic Doppler sodar winds. Part I: Theoretical Description," J. Atm and Oceanic Tech. 3, September 1986.

24. L. Kristensen and D.H. Lenschow, "An airborne laser air motion sensing system, Part II: Design criteria and measurement possibilities," J. Atm and Oceanic Tech. 4, 1987.

25. "Space-based Doppler lidar sampling strategies -- Algorithm development and simulated observation experiments," Page E-3, Final Report, NASA Contract No. NAS8-38559, Simpson Weather Associates, Inc., December 1993.

26. W.E. Baker, G.D. Emmitt, P. Robertson, R.M. Atlas, J.E. Molinari, D.A. Bowdle, J. Paegle, R.M. Hardesty, R.T. Menzies, T.N. Krishnamurti, R.A. Brown, M.J. Post, J.R. Anderson, A. C. Lorenc, T.L. Miller, and J. McElroy, "Lidar measured winds from space: An essential component for weather and climate prediction," To be published in the Bulletin of American Meteorological Society, 1995.

Report Document Page

1. Report No.	2. Government Accession No.	3. Recipient's Catalog No.

4. Title and Subtitle	5. Report Due
Analysis of Measurements for Solid State Laser Remote Lidar System	October 1994

	6. Performing Organization Code
	University of Alabama in Huntsville

7. Author(s)	8. Performing Organization Report No.
Farzin Amzajerdian	
	10. Work Unit No.

9. Performing Organization Name and Address	11. Contract or Grant No.
University of Alabama in Huntsville Huntsville, Alabama 35899	NAS8-38609, D.O. 77

	13. Type of report and Period covered
12. Sponsoring Agency Name and Address	FINAL REPORT
National Aeronautics and Space Administration Washington, D.C. 20546-001 Marshall Space Flight Center, AL 35812	14. Sponsoring Agency Code

15. Supplementary Notes

16. Abstract

17. Key Words (Suggested by Author(s))	18. Distribution Statement

19. Security Class. (of this report)	20. Security Class. (of this page)	21. No. of pages	22. Price
Unclassified	Unclassified		

NASA FORM 1626 OCT 86